

1 **POMINO-GEMS : A Research Product for Tropospheric NO<sub>2</sub> Columns from**  
2 **Geostationary Environment Monitoring Spectrometer**

3 Yuhang Zhang<sup>1</sup>, Jintai Lin<sup>1</sup>, Jhoon Kim<sup>2</sup>, Hanlim Lee<sup>3</sup>, Junsung Park<sup>3</sup>, Hyunkee Hong<sup>4</sup>, Michel Van  
4 Roozendael<sup>5</sup>, Francois Hendrick<sup>5</sup>, Ting Wang<sup>6,7</sup>, Pucui Wang<sup>6,7</sup>, Qin He<sup>8</sup>, Kai Qin<sup>8</sup>, Yongjoo Choi<sup>9</sup>,  
5 Yugo Kanaya<sup>10</sup>, Jin Xu<sup>11</sup>, Pinhua Xie<sup>7,11</sup>, Xin Tian<sup>12</sup>, Sanbao Zhang<sup>13</sup>, Shanshan Wang<sup>13</sup>, Siyang  
6 Cheng<sup>14</sup>, Xinghong Cheng<sup>14</sup>, Jianzhong Ma<sup>14</sup>, Thomas Wagner<sup>15</sup>, Robert Spurr<sup>16</sup>, Lulu Chen<sup>17</sup>, Hao  
7 Kong<sup>1</sup>, Mengyao Liu<sup>18</sup>

8 <sup>1</sup>Laboratory for Climate and Ocean-Atmosphere Studies, Department of Atmospheric and Oceanic  
9 Sciences, School of Physics, Peking University, Beijing, 100871, China

10 <sup>2</sup>Department of Atmospheric Sciences, Yonsei University, Seoul, South Korea

11 <sup>3</sup>Pukyong National University, Busan, South Korea

12 <sup>4</sup>National Institute of Environmental Research, Incheon, South Korea

13 <sup>5</sup>Belgian Institute for Space Aeronomy (BIRA-IASB), Brussels, Belgium

14 <sup>6</sup>CNRC & LAGEO, Institute of Atmospheric Physics, Chinese Academy of Sciences, Beijing, 100029,  
15 China

16 <sup>7</sup>University of Chinese Academy of Sciences, Beijing, 100049, China

17 <sup>8</sup>School of Environment and Geoinformatics, China University of Mining and Technology, Xuzhou,  
18 Jiangsu, 221116, China

19 <sup>9</sup>Department of Environmental Science, Hankuk University of Foreign Studies, Yongin, South Korea

20 <sup>10</sup>Research Institute for Global Change, Japan Agency for Marine-Earth Science and Technology  
21 (JAMSTEC), Yokohama, 2360001, Japan

22 <sup>11</sup>Key Laboratory of Environmental Optics and Technology, Anhui Institute of Optics and Fine  
23 Mechanics, Chinese Academy of Science, Hefei, 230031, China

24 <sup>12</sup>Information Materials and Intelligent Sensing Laboratory of Anhui Province, Institutes of Physical  
25 Science and Information Technology, Anhui University, Hefei, Anhui, 230601, China

26 <sup>13</sup>Shanghai Key Laboratory of Atmospheric Particle Pollution and Prevention (LAP3), Department of  
27 Environmental Science and Engineering, Fudan University, Shanghai, 200433, China

28 <sup>14</sup>State Key Laboratory of Severe Weather & Institute of Tibetan Plateau Meteorology, Chinese Academy  
29 of Meteorological Sciences, Beijing, 100081, China

30 <sup>15</sup>Max Planck Institute for Chemistry, 55020, Mainz, Germany

31 <sup>16</sup>RT Solutions Inc., Cambridge, Massachusetts, 02138, USA

32 <sup>17</sup>College of Urban and Environmental Sciences, Peking University, Beijing, 100871, China

33 <sup>18</sup>R&D Satellite Observations Department, Royal Netherlands Meteorological Institute, De Bilt, the  
34 Netherlands

35 *Correspondence to:* Jintai Lin ([linjt@pku.edu.cn](mailto:linjt@pku.edu.cn))

36 **Abstract**

37 Tropospheric vertical column densities (VCDs) of nitrogen dioxide (NO<sub>2</sub>) retrieved from sun-  
38 synchronous satellite instruments have provided abundant NO<sub>2</sub> data for environmental studies, but such

39 data are limited by retrieval uncertainties and insufficient temporal sampling (e.g., once a day). The  
40 Geostationary Environment Monitoring Spectrometer (GEMS) launched in February 2020 monitors NO<sub>2</sub>  
41 at an unprecedented hourly resolution during the daytime. Here we present a research product for  
42 tropospheric NO<sub>2</sub> VCDs, referred to as POMINO-GEMS. We develop a hybrid retrieval method  
43 combining GEMS, TROPOMI and GEOS-CF data to generate hourly tropospheric NO<sub>2</sub> slant column  
44 densities (SCDs). We then derive tropospheric NO<sub>2</sub> air mass factors (AMFs) with explicit corrections for  
45 surface reflectance anisotropy and aerosol optical effects, through parallelized pixel-by-pixel radiative  
46 transfer calculations. Prerequisite cloud parameters are retrieved with the O<sub>2</sub>-O<sub>2</sub> algorithm by using  
47 ancillary parameters consistent with those used in NO<sub>2</sub> AMF calculations.

48 Initial retrieval of POMINO-GEMS tropospheric NO<sub>2</sub> VCDs for June–August 2021 exhibits strong  
49 hotspot signals over megacities and distinctive diurnal variations over polluted and clean areas.  
50 POMINO-GEMS NO<sub>2</sub> VCDs agree with the POMINO-TROPOMI v1.2.2 product ( $R = 0.98$ , and NMB  
51 = 4.9%) over East Asia, with slight differences associated with satellite viewing geometries and cloud  
52 and aerosol properties affecting the NO<sub>2</sub> retrieval. POMINO-GEMS also shows good agreement with  
53 OMNO2 v4 ( $R = 0.87$ , and NMB = -16.8%) and GOME-2 GDP 4.8 ( $R = 0.83$ , and NMB = -1.5%) NO<sub>2</sub>  
54 products. POMINO-GEMS shows small biases against ground-based MAX-DOAS NO<sub>2</sub> VCD data at  
55 nine sites (NMB = -11.1%) with modest or high correlation in diurnal variation at six urban and suburban  
56 sites ( $R$  from 0.60 to 0.96). The spatiotemporal variation of POMINO-GEMS correlates well with  
57 mobile-car MAX-DOAS measurements in the Three Rivers' Source region on the Tibetan Plateau ( $R =$   
58 0.81). Surface NO<sub>2</sub> concentrations estimated from POMINO-GEMS VCDs are consistent with  
59 measurements from the Ministry of Ecology and Environment of China for spatiotemporal variation ( $R$   
60 = 0.78, and NMB = -26.3%) as well as diurnal variation at all, urban, suburban and rural sites ( $R \geq 0.96$ ).  
61 POMINO-GEMS data will be made freely available for users to study the spatiotemporal variations,  
62 sources and impacts of NO<sub>2</sub>.

## 63 **1. Introduction**

64 Tropospheric nitrogen dioxide (NO<sub>2</sub>) is an important air pollutant. It threatens human health, and  
65 contributes to the formation of tropospheric ozone (O<sub>3</sub>) and nitrate aerosols (Crutzen, 1970; Shindell et  
66 al., 2009; Hoek et al., 2013; Chen et al., 2022). Satellite instruments provide observations of tropospheric  
67 NO<sub>2</sub> on a global scale, and they have been extensively used to estimate emissions of nitrogen oxides

68 ( $\text{NO}_x = \text{NO} + \text{NO}_2$ ) (Lin and Mcelroy, 2011; Beirle et al., 2011; Gu et al., 2014; Kong et al., 2022a),  
69 surface  $\text{NO}_2$  concentrations (Wei et al., 2022; Cooper et al., 2022), trends and variabilities (Richter et al.,  
70 2005; Cui et al., 2016; Krotkov et al., 2016; Van Der A et al., 2017), and impacts on human health and  
71 environment (Chen et al., 2021).

72 To date, most spaceborne instruments for  $\text{NO}_2$  measurements, including the Global Ozone  
73 Monitoring Instrument (GOME) (Burrows, 1999), the Ozone Monitoring Instrument (OMI) (Levelt et  
74 al., 2006), the Global Ozone Monitoring Experiment 2 (GOME-2) (Callies et al., 2000) and the  
75 TROPOspheric Monitoring Instrument (TROPOMI) (Veefkind et al., 2012), are mounted on sun-  
76 synchronous low Earth orbit (LEO) satellites. These instruments passively measure backscattered  
77 radiance from the Earth's atmosphere, and measurements at each ground location are done 1–2 times a  
78 day. The Geostationary Environment Monitoring Spectrometer (GEMS) on board the Geostationary  
79 Korea Multi-Purpose Satellite-2B (GK-2B) was successfully launched in February 2020. The instrument  
80 provides measurements of  $\text{NO}_2$  and other pollutants in the daytime on an hourly basis (Kim et al., 2020).  
81 It complements LEO satellite observations by providing a more comprehensive picture of the daytime  
82 evolution of  $\text{NO}_2$ .

83 There are three successive stages in the retrieval of tropospheric  $\text{NO}_2$  vertical column densities  
84 (VCDs) in the UV-Vis range based on satellite observations. The first step is to retrieve total  $\text{NO}_2$  slant  
85 column densities (SCDs) with spectral fitting techniques, such as the Differential Optical Absorption  
86 Spectroscopy (DOAS). The SCD represents the abundance of  $\text{NO}_2$  along the effective light path from  
87 the sun through the atmosphere to the satellite instrument. Next, the contributions from stratospheric  $\text{NO}_2$   
88 to the total SCDs are removed in order to obtain tropospheric SCDs. Finally, the tropospheric SCDs are  
89 converted to VCDs using calculated air mass factors (AMFs). The AMF calculations are highly sensitive  
90 to the observation geometry, cloud parameters, aerosols, surface conditions and the shape of the  $\text{NO}_2$   
91 vertical distribution. Over polluted areas, errors in the retrieved tropospheric  $\text{NO}_2$  VCDs are dominated  
92 by the uncertainties in AMF calculations (Boersma et al., 2004; Lorente et al., 2016) associated with  
93 aerosol optical effects, surface reflectance and a priori  $\text{NO}_2$  vertical profiles (Zhou et al., 2010; Lin et al.,  
94 2014; Lin et al., 2015; Vasilkov et al., 2016; Lorente et al., 2018; Liu et al., 2019; Liu et al., 2020;  
95 Vasilkov et al., 2021).

96 The official GEMS retrieval algorithm for tropospheric  $\text{NO}_2$  VCDs is developed by Lee et al. (2020).

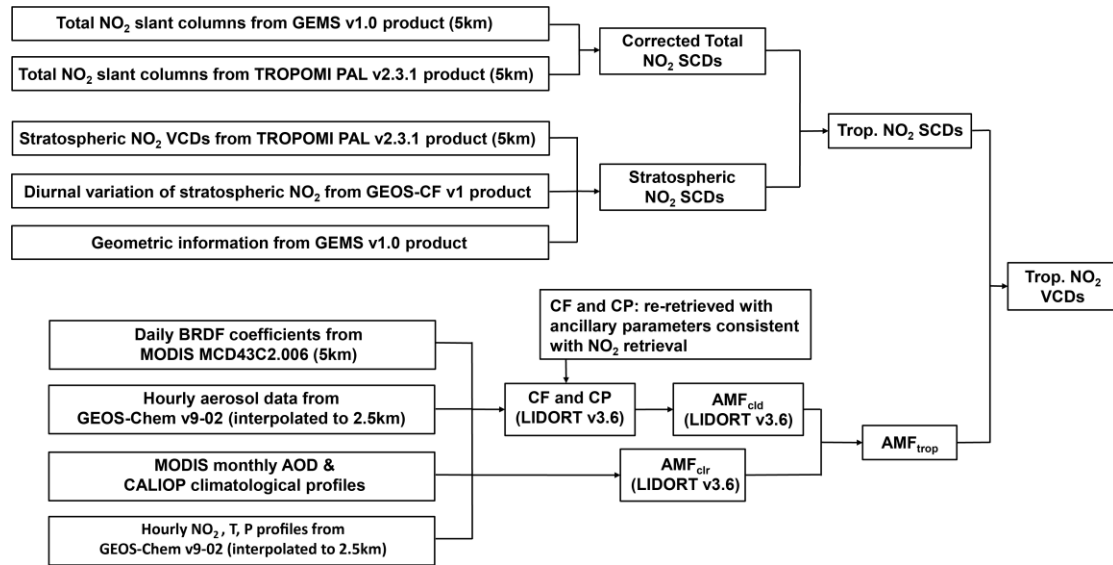
97 The total NO<sub>2</sub> SCDs are retrieved using the DOAS technique. They are then converted to total NO<sub>2</sub> VCDs  
98 by using a precomputed look-up table of box AMFs based on the linearized pseudo-spherical scalar and  
99 vector discrete ordinate radiative transfer code (VLIDORT) version 2.6. Finally, stratosphere-  
100 troposphere separation (STS) is performed to derive tropospheric NO<sub>2</sub>. Validation results have shown the  
101 overall capability of the official GEMS NO<sub>2</sub> algorithm (Kim et al., 2023), but several problems are also  
102 reported, such as overestimation of total NO<sub>2</sub> SCDs and tropospheric NO<sub>2</sub> VCDs, and some degree of  
103 striping in NO<sub>2</sub> retrieval data.

104 In this study, we present a research product which we name as POMINO-GEMS. This product is  
105 built upon our Peking University OMI NO<sub>2</sub> (POMINO) algorithm which focuses on the tropospheric  
106 AMF calculations and has been applied to OMI and TROPOMI (Lin et al., 2014; Lin et al., 2015; Liu et  
107 al., 2019; Liu et al., 2020; Zhang et al., 2022). Here we extend the AMF calculation by constructing a  
108 hybrid method to estimate tropospheric SCDs for GEMS. The hybrid method makes use of the total  
109 SCDs from the official GEMS product, total SCDs and stratospheric VCDs from the official TROPOMI  
110 product, as well as hourly stratospheric VCD data from the NASA Global Earth Observing System  
111 Composition Forecast (GEOS-CF) v1 product. We validate our initial set of retrieval results for  
112 tropospheric NO<sub>2</sub> VCDs in June-July-August (JJA) 2021, by using independent data of tropospheric NO<sub>2</sub>  
113 from the POMINO-TROPOMI v1.2.2, OMNO2 v4 and GOME-2 GDP 4.8 products, ground-based and  
114 mobile-car MAX-DOAS measurements, and surface concentration observations from the Ministry of  
115 Ecology and Environment (MEE) of China. We provide a simplified estimate of retrieval errors in the  
116 end.

## 117 **2. Method and data**

### 118 **2.1 Construction of POMINO-GEMS retrieval algorithm**

119 Figure 1 shows the flow chart of POMINO-GEMS retrieval algorithm. There are two essential steps.  
120 The first is to calculate tropospheric NO<sub>2</sub> SCDs on an hourly basis, through fusion of total SCDs from  
121 the official GEMS v1.0 L2 NO<sub>2</sub> product, total SCDs and stratospheric VCDs from the TROPOMI PAL  
122 v2.3.1 L2 NO<sub>2</sub> product, and diurnal variations of stratospheric NO<sub>2</sub> from the GEOS-CF v1 product. We  
123 then calculate tropospheric NO<sub>2</sub> AMFs to convert SCDs to VCDs.



124  
125 **Figure 1. Flow chart of POMINO-GEMS retrieval algorithm. The numbers in the boxes, such as 5 km, refer**  
126 **to horizontal resolutions.**

### 127 2.1.1 GEMS NO<sub>2</sub> and cloud data

128 The GEMS instrument is on board the GK-2B satellite locating at 128.2°E over the equator (Kim  
129 et al., 2020). The spectral wavelength range of GEMS is 300-500 nm, covering main absorption spectra  
130 of aerosols and trace gases. The nominal spatial resolution is typically 7 km × 8 km for gases and 3.5 km  
131 × 8 km for aerosols in the eastern and central scan domains; however, the north-south spatial resolution  
132 can exceed 25 km in the western side. The whole field of view (FOV) covers about 20 Asian countries  
133 within latitudes 5°S to 45°N and longitudes 80°E to 152°E. Given the variation of solar zenith angle  
134 (SZA), there are four scan scenarios moving from east to west, including Half East (HE), Half Korea  
135 (HK), Full Central (FC) and Full West (FW). It takes 30 minutes (for example, 00:45 – 01:15 UTC) for  
136 GEMS to scan its full coverage during each scenario, and the next 30 minutes to transmit data to the  
137 ground data center. The number of hourly GEMS observations per day varies from 6 in winter to 10 in  
138 summer, corresponding to the annual movement of subsolar points relative to the Earth.

139 We take hourly total (stratospheric + tropospheric) NO<sub>2</sub> SCDs from the official GEMS v1.0 L2 NO<sub>2</sub>  
140 product, and convert them to 0.05° × 0.05° gridded data by means of an area-weighted oversampling  
141 technique. The value of each grid cell is the mean value of pixel-based GEMS observations weighted by  
142 the ratio of the overlap area of each pixel to the area of grid cell. We also use continuum reflectance data  
143 (i.e., spectrally smooth reflectance from molecular and aerosol extinction as well as surface reflectance  
144 effects) and O<sub>2</sub>-O<sub>2</sub> SCDs from the official GEMS v1.0 L2 cloud product to re-calculate cloud parameters

145 as a prerequisite for tropospheric NO<sub>2</sub> AMF calculations. Details of the GEMS retrievals can be found  
146 in the algorithm theoretical basis document (ATBD) (Lee et al., 2020).

### 147 **2.1.2 TROPOMI, OMI and GOME-2 NO<sub>2</sub> data**

148 Table S1 compares the basic information of GEMS with those of TROPOMI, OMI and GOME-2  
149 instruments. In this study, TROPOMI data are used for derivation of POMINO-GEMS NO<sub>2</sub> VCDs, and  
150 data from all of the three LEO instruments are used for comparison with POMINO-GEMS.

151 We use total NO<sub>2</sub> SCDs and stratospheric NO<sub>2</sub> VCDs from the official TROPOMI PAL v2.3.1 L2  
152 NO<sub>2</sub> product, and convert them to 0.05° × 0.05° gridded data, again using an area-weighted oversampling  
153 technique. Details of TROPOMI total SCD retrievals and stratospheric VCD calculations are given in  
154 the TROPOMI ATBD (Van Geffen et al., 2022a). The TROPOMI PAL product is reprocessed with  
155 TROPOMI NO<sub>2</sub> data processor v2.3.1 for the period from 1 May 2018 to 14 November 2021; it will be  
156 replaced by the full mission reprocessing with NO<sub>2</sub> processor v2.4.0 in the future (Eskes et al., 2021).  
157 The most important improvement in this PAL product upon the previous OFFL v1.3 is the replacement  
158 of the FRESCO-S algorithm with the FRESCO-wide cloud retrieval algorithm, which leads to higher,  
159 more reasonable cloud pressure (CP) estimates and substantial increases in tropospheric NO<sub>2</sub> VCDs (by  
160 20% – 50%) over polluted regions like Eastern China in winter (Eskes et al., 2021; Van Geffen et al.,  
161 2022b).

162 We use the POMINO-TROPOMI v1.2.2, OMNO2 v4 (Lamsal et al., 2021) and GOME-2 GDP 4.8  
163 (Valks et al., 2019) tropospheric NO<sub>2</sub> VCD products to compare with POMINO-GEMS results. The  
164 previous POMINO-TROPOMI v1 data show higher accuracy in polluted situations and improved  
165 consistency with MAX-DOAS measurements when compared with the official TM5-MP-DOMINO  
166 (OFFLINE) product (Liu et al., 2020). POMINO-TROPOMI v1.2.2 improves upon v1 by (1) using  
167 tropospheric NO<sub>2</sub> SCD and CP data from the updated TROPOMI PAL v2.3.1 NO<sub>2</sub> product, (2)  
168 interpolating the daily NO<sub>2</sub>, pressure, temperature and aerosol vertical profiles from nested GEOS-Chem  
169 (v9-02) simulations into a horizontal grid of 2.5 km x 2.5 km for subsequent tropospheric AMF  
170 calculations, and (3) including several minor bug fixes.

171 We select valid satellite pixels following common practice. For the daily POMINO-TROPOMI  
172 v1.2.2 L2 NO<sub>2</sub> product, we exclude pixels with SZA or viewing zenith angle (VZA) greater than 80°,  
173 high albedos caused by ice or snow on the ground, quality flag values (from the TROPOMI PAL v2.3.1

174 product) less than 0.5 or cloud radiance fraction (CRF) greater than 50%, and then map the valid data to  
175 a  $0.05^\circ \times 0.05^\circ$  grid. For the daily OMNO2 v4 L2 NO<sub>2</sub> product, we exclude pixels with SZA or VZA  
176 greater than 80°, with scene Lambert-equivalent reflectivity (LER) greater than 0.3, affected by row  
177 anomaly (XTrackQualityFlags is not zero), marked without quality assurance (vcdQualityFlag is not an  
178 even integer) or with CRF greater than 50%, and then map the valid data to a  $0.25^\circ \times 0.25^\circ$  grid. For the  
179 daily GOME-2 GDP 4.8 L2 NO<sub>2</sub> product, we exclude pixels with latitude greater than 70°, SZA greater  
180 than 80°, failed retrieval (NO2Tropo\_Flag is set to 1 or 2) or with CRF greater than 50%, and then map  
181 the valid data to a  $0.5^\circ \times 0.5^\circ$  grid.

### 182 **2.1.3 GEOS-CF stratospheric NO<sub>2</sub> data**

183 The NASA GEOS-CF system combines the Global Earth Observing System (GEOS) weather  
184 analysis and forecasting system with GEOS-Chem v12.0.1 chemistry module (<http://geoschem.org>) to  
185 provide near real-time estimates of atmospheric compositions with daily 5-day forecasts. Detailed  
186 information of the model, including chemistry, emissions and deposition, and evaluation of the GEOS-  
187 CF tropospheric simulation and forecast skill are presented in Keller et al. (2021). In particular, the  
188 GEOS-Chem v12.0.1 chemistry scheme includes online stratospheric chemistry that is fully coupled with  
189 tropospheric chemistry through the Unified tropospheric-stratospheric Chemistry eXtension (UCX)  
190 mechanism (Eastham et al., 2014). The GEOS-CF stratospheric results are consistent with satellite  
191 observations, albeit with notable underestimation of NO<sub>x</sub> and HNO<sub>3</sub> in the polar regions (Knowland et  
192 al., 2022b).

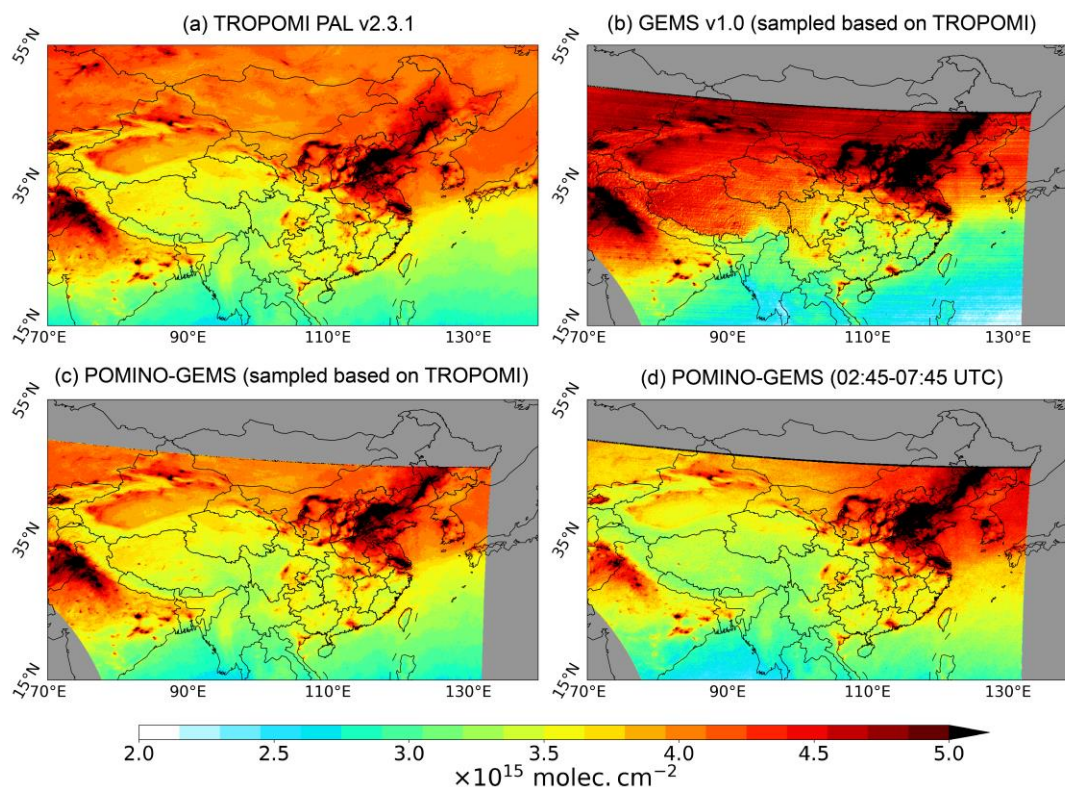
193 The GEOS-CF outputs have a horizontal resolution of  $0.25^\circ \times 0.25^\circ$  and a temporal resolution of 1  
194 hour for NO<sub>2</sub> and other ancillary data used here (Knowland et al., 2022a). We convert instantaneous  
195 stratospheric NO<sub>2</sub> volume mixing ratio in dry air at each hour (e.g., 00:00 UTC) into  $0.05^\circ \times 0.05^\circ$   
196 gridded vertical column densities based on estimated tropopause information in GEOS-CF v1. In Section  
197 2.1.5, we first evaluate GEOS-CF v1 stratospheric NO<sub>2</sub> VCDs with those of TROPOMI PAL v2.3.1  
198 product, and then calculate hourly stratospheric NO<sub>2</sub> VCDs by combining GEOS-CF v1 data for each  
199 hour and TROPOMI PAL v2.3.1 stratospheric NO<sub>2</sub> VCD data in the early afternoon.

### 200 **2.1.4 Calculation of total NO<sub>2</sub> SCDs**

201 We use TROPOMI data to correct GEMS total NO<sub>2</sub> SCDs, given known issues in GEMS data.  
202 Specifics for the NO<sub>2</sub> SCD retrieval of TROPOMI PAL v2.3.1 and GEMS v1.0 operational products are

203 provided in Table S2.

204 Figure 2a and b show the spatial distribution of monthly mean total NO<sub>2</sub> geometric column densities  
205 (GCDs, calculated as SCDs divided by geometric AMFs) in June 2021 from TROPOMI PAL v2.3.1 and  
206 GEMS v1.0, respectively. The horizontal resolution is 0.05° × 0.05°. The GCDs are used to compare the  
207 two products after removing the effect of measurement geometry. Matching for each day between hourly  
208 GEMS observations and the TROPOMI data at the closest observation time is done to ensure temporal  
209 compatibility. The figures show that the spatial pattern of GEMS GCDs agrees well with that of  
210 TROPOMI, with high values over the North China Plain (NCP) and Northwestern India, as well as major  
211 metropolitan clusters such as Seoul and the Yangtze River Delta (YRD). However, there are two  
212 systematic problems in GEMS GCDs. First, the GEMS GCD values are abnormally high over the  
213 northern and northwestern parts of GEMS FOV, especially over Mongolia, Qinghai, Inner Mongolia,  
214 Xinjiang and Tibet of China. Second, west-east stripes exist over the whole domain, similar to the  
215 spurious across-track variability issue for OMI. This stripe issue exists at all hours (Figure S1). It is likely  
216 associated with the specific scan modes of GEMS, as well as periodically occurring bad pixels as one of  
217 remaining calibration issues (Boersma et al., 2011; Lee et al., 2023).



218  
219 **Figure 2. Spatial distribution of monthly mean total NO<sub>2</sub> GCDs on a 0.05° × 0.05° grid in June 2021. (a) The**  
220 **TROPOMI PAL v2.3.1 product, (b) the official GEMS v1.0 product that spatiotemporally matches with**  
221 **TROPOMI, (c) the corrected POMINO-GEMS product that spatiotemporally matches with TROPOMI,**



222 **and (d) the corrected POMINO-GEMS product averaged over 02:45 – 07:45 UTC. Note the range of the**  
223 **color bar is  $2.0 - 5.0 \times 10^{15}$  molec. cm<sup>-2</sup>. The regions in grey mean there are no valid observations.**

224 To correct the two issues in the GEMS official total NO<sub>2</sub> SCD product, we combine GEMS and  
225 TROPOMI observations to obtain hourly  $0.05^\circ \times 0.05^\circ$  corrected total NO<sub>2</sub> SCDs for each day using Eqs.  
226 (1) and (2):

$$227 \quad \Delta\text{GCD} = \frac{1}{n} \sum_{i=1}^n (\text{GCD}_{\text{total},h_i}^{\text{TROPOMI}} - \text{GCD}_{\text{total},h_i}^{\text{GEMS}}) \quad (1)$$

$$228 \quad \text{SCD}_{\text{total},h}^{\text{corrected}} = \text{SCD}_{\text{total},h}^{\text{GEMS}} + \Delta\text{GCD} \times \text{AMF}_{\text{geo}_h}^{\text{GEMS}} \quad (2)$$

229 In Eqs. (1) and (2), index  $h$  represents the hour of GEMS observations on each day;  $h_i$  the hour  
230 when both GEMS and TROPOMI have valid observations for the same grid cell; and  $n$  the number of  $h_i$ .  
231 The value of  $n$  is 1 or 2 depending on the overpass times of TROPOMI. There are two steps in the  
232 correction process. First, we calculate a geometry-independent correction map for each day using total  
233 NO<sub>2</sub> GCDs from GEMS and TROPOMI that match spatially and temporally (Eq. (1)). We use the  
234 absolute difference instead of a scaling factor as a simple correction. We then apply the correction to the  
235 original GEMS total NO<sub>2</sub> SCDs at each hour on the same day, with the diurnal variation in AMF  
236 associated with measurement geometry accounted for (Eq. (2)).

237 In Eq. (2), we implement a simple geometric correction (concerning SZAs and VZAs) for AMFs  
238 instead of using the actual AMFs; the latter could account for the differences in relative azimuth angles  
239 and other factors. Specific derivation of this assumption is given in Section 1 of the Supplement  
240 Information (SI). The correction is assumed to be acceptable with an extra uncertainty introduced to the  
241 total NO<sub>2</sub> SCDs, as will be further discussed in Section 3.5.

242 Figure 2c shows the monthly mean corrected POMINO-GEMS total NO<sub>2</sub> GCDs in June 2021 after  
243 spatial and temporal matching with TROPOMI. The corrected GCD values in the northern GEMS FOV  
244 are much reduced compared with those in the original GEMS data. Moreover, most stripe-like patterns  
245 are removed in the corrected GCDs. Figure 2d is similar to Fig. 2c but for GCDs averaged over 02:45 –  
246 07:45 UTC in June 2021. Figure S3 further compares the original GEMS and POMINO-GEMS total  
247 NO<sub>2</sub> GCDs at each hour in JJA 2021, showing similar improvements as well. The differences between  
248 Figure 2c and d indicate the influence of different sampling hours combined with the daily correction  
249 map. Specifically, the correction value of each grid cell is calculated at the specific hour when both  
250 GEMS and TROPOMI have valid observations, but this value is applied to original GEMS SCDs at all

251 hours.

252 Our correction method is done for each grid cell. We tested other correction methods by applying  
253 the same correction value to grid cells within a  $20^\circ \times 20^\circ$  domain, at the same latitude, or at the same  
254 longitude. These alternative methods can reduce the high bias over the northern and northwestern GEMS  
255 FOV to various extents, but cannot remove the stripes (not shown). We also note that our simple  
256 correction is a temporary solution before the aforementioned systematic problems in the official GEMS  
257 SCD retrieval are solved by improving spectral fitting. In Sections 3.3 and 3.4, we compare the diurnal  
258 variations of tropospheric NO<sub>2</sub> VCDs based on corrected and uncorrected GEMS SCDs.

### 259 **2.1.5 Calculation of stratospheric and tropospheric NO<sub>2</sub> SCDs**

260 We construct a dataset of hourly stratospheric NO<sub>2</sub> SCDs at  $0.05^\circ \times 0.05^\circ$  by using TROPOMI PAL  
261 v2.3.1 stratospheric NO<sub>2</sub> VCDs, diurnal variation of stratospheric NO<sub>2</sub> VCDs provided by GEOS-CF v1  
262 product, and GEMS geometric AMFs.

263 Figure S4 shows the comparison results between GEOS-CF v1 and TROPOMI PAL v2.3.1  
264 stratospheric NO<sub>2</sub> VCDs in June 2021. Consistent spatial and temporal sampling is done.  $N$  is the total  
265 number of matched  $0.05^\circ \times 0.05^\circ$  grid cells. The stratospheric VCDs from both products vary in the range  
266 of  $2 - 5 \times 10^{15}$  molec. cm<sup>-2</sup>, with spatiotemporal correlation of 0.99, linear regression slope of 0.99 and  
267 normalized mean bias (NMB) of 0.02%. This consistency provides confidence on the overall reliability  
268 of GEOS-CF stratospheric NO<sub>2</sub> data.

269 First, we calculate stratospheric NO<sub>2</sub> VCDs at a reference hour for each day using Eqs. (3) and (4):

$$270 \quad \text{ratio}_{h_0}^h = \frac{\text{VCD}_{\text{strat},h}^{\text{GEOS-CF}}}{\text{VCD}_{\text{strat},h_0}^{\text{GEOS-CF}}} \quad (3)$$

$$271 \quad \text{VCD}_{\text{strat},h_0} = \frac{1}{n} \sum_{i=1}^n \frac{\text{VCD}_{\text{strat},h_i}^{\text{TROPOMI}}}{\text{ratio}_{h_0}^{h_i}} \quad (4)$$

272 Here, Eq. (3) defines the ratio of GEOS-CF stratospheric NO<sub>2</sub> at hour  $h$  to that at the reference hour  
273  $h_0$ , which is chosen to be 01:00 UTC (Figure S5). In Eq. (4),  $h_i$  represents the observation time of every  
274 TROPOMI orbit that overlaps with GEMS FOV, and  $n$  the number of  $h_i$  for each grid cell.

275 Second, we use the ratio from a given time  $h$  to  $h_0$  and stratospheric NO<sub>2</sub> VCDs at  $h_0$  to derive  
276 stratospheric NO<sub>2</sub> VCDs at  $h$  for each day (Eq. (5)).

$$277 \quad \text{VCD}_{\text{strat},h} = \text{VCD}_{\text{strat},h_0} \times \text{ratio}_{h_0}^h \quad (5)$$

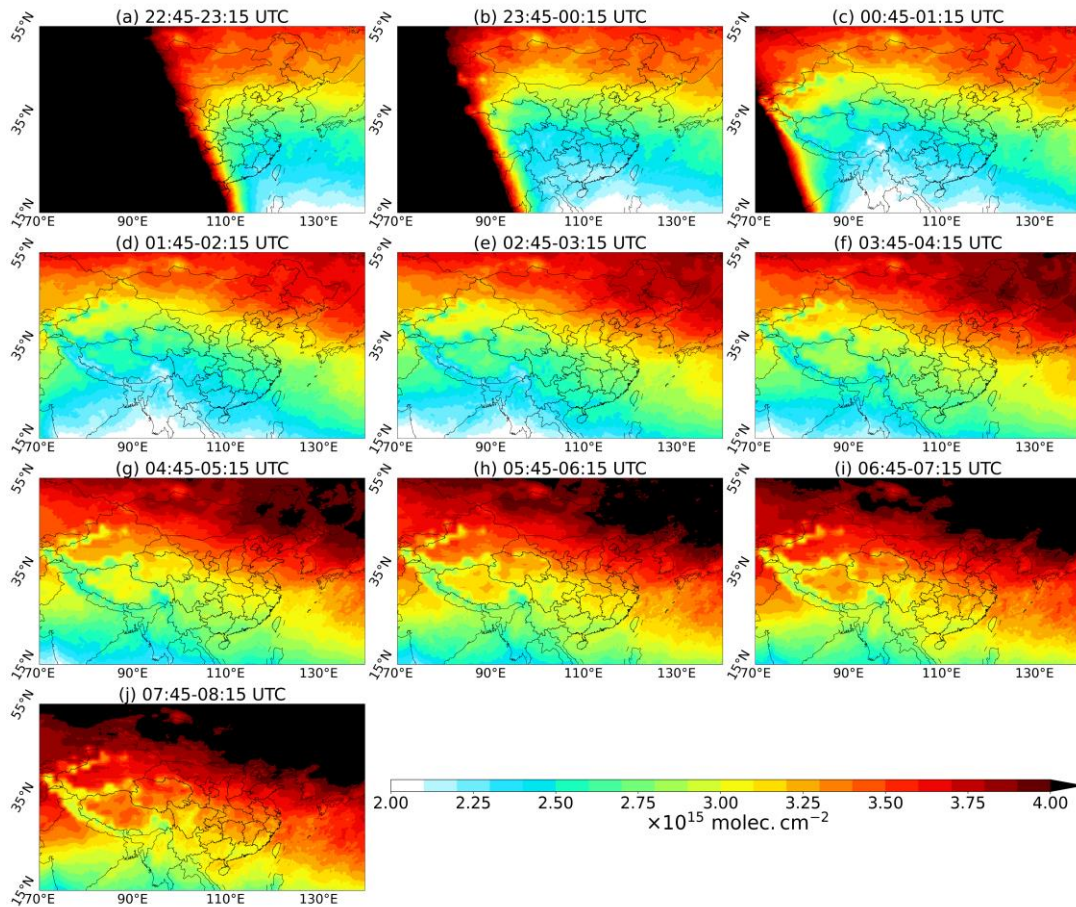
278 Figure 3 shows the derived monthly mean stratospheric NO<sub>2</sub> VCDs at each hour in June 2021 on a

279  $0.05^\circ \times 0.05^\circ$  grid. The abrupt decrease of stratospheric  $\text{NO}_2$  VCDs after sunrise is caused by resumed  
 280 photochemical conversion of  $\text{NO}_2$  to  $\text{NO}$  (Li et al., 2021b). There is a strong meridional gradient of  
 281 stratospheric  $\text{NO}_2$  in the daytime, with the higher values in the north associated with longer lifetimes.  
 282 The stratospheric  $\text{NO}_2$  increase quasi-linearly during the daytime; linear regression to the mean  
 283 stratospheric  $\text{NO}_2$  VCDs over the whole domain from 01:45 to 07:45 UTC results in an increasing rate  
 284 of  $(1.12 \pm 0.03) \times 10^{14}$  molec.  $\text{cm}^{-2} \text{h}^{-1}$ . This result is consistent with previous work showing quasi-linear  
 285 growth in the daytime at rates of  $0.5 - 2 \times 10^{14}$  molec.  $\text{cm}^{-2} \text{h}^{-1}$  depending on latitude and season (Li et  
 286 al., 2021b; Dirksen et al., 2011).

287 Finally, we use GEMS geometric AMFs to convert the stratospheric  $\text{NO}_2$  VCDs to SCDs at each  
 288 hour, and then subtract them from the total SCDs to obtain tropospheric SCDs (Eqs. (6) and (7)). In the  
 289 stratosphere, the geometric AMFs are essentially the same as the actual AMFs

$$290 \quad \text{SCD}_{\text{strat},h} = \text{VCD}_{\text{strat},h} \times \text{AMF}_{\text{geo}_h}^{\text{GEMS}} \quad (6)$$

$$291 \quad \text{SCD}_{\text{trop},h}^{\text{GEMS}^*} = \text{SCD}_{\text{total},h}^{\text{corrected}} - \text{SCD}_{\text{strat},h} \quad (7)$$



292  
 293 **Figure 3. Spatial distribution of POMINO-GEMS derived monthly mean stratospheric  $\text{NO}_2$  VCDs at each**  
 294 **hour on a  $0.05^\circ \times 0.05^\circ$  grid in June 2021. Note the range of the color bar is  $2.0 - 4.0 \times 10^{15}$  molec.  $\text{cm}^{-2}$ .**

### 2.1.6 Calculation of tropospheric AMFs

Tropospheric NO<sub>2</sub> AMF is dependent on three factors as defined in Palmer et al. (2001): the viewing geometry, the scattering weights describing the sensitivity of the backscattered spectrum to the abundance of the absorber, and a priori NO<sub>2</sub> vertical profile (Eq. (8)).

$$\text{AMF} = \text{AMF}_G \int_0^{z_T} w(z)S(z)dz \quad (8)$$

In Eq. (8), AMF<sub>G</sub> is the geometric AMF and a function of SZA and VZA,  $w(z)$  the scattering weight at altitude  $z$ ,  $S(z)$  the normalized vertical profile of NO<sub>2</sub> number density, and  $z_T$  the tropopause. Following Yang et al. (2023), we refer to  $\int_0^{z_T} w(z)S(z)dz$  as the scattering correction factor for discussion in Section 3.2. For tropospheric AMF calculations (Figure 1), we use a parallelized AMFv6 package driven by LIDORT version 3.6; this is similar to the one used in our previous POMINO products (Lin et al., 2014; Lin et al., 2015; Liu et al., 2019) but with modifications to adapt to the geostationary observing characteristics and high spatiotemporal resolution of GEMS. We take daily BRDF coefficients with a horizontal resolution of 5 km from the MODIS MCD43C2.006 dataset (Lucht et al., 2000) to account for the anisotropy of surface reflectance over land and coastal ocean regions, and OMLER v3 albedo over open ocean (Zhou et al., 2010; Lin et al., 2014; Liu et al., 2020). Hourly-varying aerosol parameters, a priori NO<sub>2</sub> profiles, temperature profiles and pressure profiles are interpolated from nested GEOS-Chem (v9-02) results to a horizontal resolution of 2.5 km, using the Piecewise Cubic Hermite Interpolating Polynomial (PCHIP) method. Furthermore, we deploy AOD observations from the MODIS/Aqua Collection 6.1 MYD04\_L2 dataset to constrain model-simulated AOD on a monthly basis (Lin et al., 2014; Lin et al., 2015; Liu et al., 2019; Liu et al., 2020); and we use a self-constructed monthly climatological dataset of aerosol extinction profiles based on CALIOP L2 data over 2007-2015 to constrain modeled aerosol vertical profiles on a monthly climatology basis (Liu et al., 2019). We retrieve cloud parameters based on O<sub>2</sub>-O<sub>2</sub> SCDs and continuum reflectances from the official GEMS v1.0 cloud product, using ancillary parameters consistent with those used in NO<sub>2</sub> AMF calculations. Instead of relying on a look-up table (LUT), we conduct pixel-by-pixel radiative transfer calculations with the parallelized AMFv6 package. The independent pixel approximation (IPA) is assumed for cloud-contaminated pixels as in other algorithms. Finally, we use the AMF data to convert tropospheric NO<sub>2</sub> SCDs to VCDs.

Invalid pixels in the POMINO-GEMS product are filtered based on the following criteria. We

324 exclude pixels with SZA or VZA greater than 80°, or with the ground covered by ice or snow. To  
325 minimize cloud contamination, we exclude pixels with CRF greater than 50%.

## 326 2.2 Estimation of surface NO<sub>2</sub> concentrations

327 In order to validate satellite NO<sub>2</sub> products with surface concentration measurements from MEE, we  
328 convert tropospheric NO<sub>2</sub> VCDs from satellite products on a 0.05° × 0.05° grid to surface NO<sub>2</sub> mass  
329 concentrations using GEOS-Chem simulated NO<sub>2</sub> vertical profiles and the box heights of the lowest  
330 model layer (Eq. (9)).

$$331 \quad C_{\text{surf}} = \text{VCD}_{\text{trop}}^{\text{SAT}} \times R^{\text{GC}} \times \frac{M}{N \times H^{\text{GC}}} \times 2 \quad (9)$$

332 In Eq. (9),  $C_{\text{surf}}$  represents the estimated surface NO<sub>2</sub> mass concentration in  $\mu\text{g m}^{-3}$ ,  $\text{VCD}_{\text{trop}}^{\text{SAT}}$  the  
333 satellite tropospheric VCD in molecules.  $\text{m}^{-2}$ ,  $R^{\text{GC}}$  the GEOS-Chem simulated hourly ratio of NO<sub>2</sub> sub-  
334 column in the lowest layer to the total tropospheric column,  $M$  the NO<sub>2</sub> molar mass in  $\mu\text{g mol}^{-1}$ ,  $N$  the  
335 Avogadro constant, and  $H^{\text{GC}}$  the box height of the lowest layer in m. The thickness of the lowest layer  
336 of GEOS-Chem (about 130 m) is too large for the layer average NO<sub>2</sub> mass concentration to represent  
337 that near the ground (Liu et al., 2018a); thus the derived concentration is multiplied by a factor of 2 to  
338 roughly account for the vertical gradient from the height of ground instrument to the center of the model  
339 layer. However, the constant correction factor of 2 neglects the diurnal variation of NO<sub>2</sub> vertical gradient,  
340 which is related to the diurnal variation of planetary boundary layer (PBL) heights. This issue is discussed  
341 in detail in Section 3.4.

## 342 2.3 Ground-based MAX-DOAS measurements

343 We use ground-based MAX-DOAS NO<sub>2</sub> measurements, together with POMINO-TROPOMI v1.2.2,  
344 OMNO2 v4 and GOME-2 GDP 4.8 NO<sub>2</sub> products, to validate the POMINO-GEMS retrieval results. The  
345 types, geolocations and observation times of MAX-DOAS stations are summarized in Table S3, and the  
346 location of each site is shown in Figure S6. Details of each site are described in Section 2 of the SI.  
347 Kanaya et al. (2014) and Hendrick et al. (2014) have discussed the error in MAX-DOAS NO<sub>2</sub> retrieval:  
348 uncertainties from a priori aerosol and NO<sub>2</sub> profiles are the largest source by 10% – 14%, and the total  
349 retrieval uncertainty is typically 12% – 17%.

350 To ensure sampling consistency in time, we average all valid MAX-DOAS measurements within  
351 each observation period of GEMS (i.e., 30 minutes) for hourly comparison, and within  $\pm 1.5$  h of

352 TROPOMI, OMI and GOME-2 overpass time for daily comparison. Following the procedures in  
353 previous studies (Lin et al., 2014; Liu et al., 2020), we exclude all matched MAX-DOAS data for which  
354 the standard deviation exceeds 20% of the mean value to minimize the influence of local events. To  
355 ensure sampling consistency in space, we select valid satellite pixels within 5 km of MAX-DOAS sites  
356 for POMINO-GEMS and POMINO-TROPOMI v1.2.2, 25 km for OMNO2 v4 and 50 km for GOME-2  
357 GDP 4.8, and conduct spatial averaging. The Grubbs statistical test, which is used to detect outliers in a  
358 univariate data set assumed to exhibit normal distribution (Grubbs, 1950), is performed to exclude  
359 outliers in both MAX-DOAS and satellite data before comparison. Only one data pair from Fudan  
360 University site is identified as an outlier and removed (Figure S7), and we get 1348 matched hourly data  
361 pairs in total.

#### 362 **2.4 Mobile-car MAX-DOAS measurements**

363 We use tropospheric NO<sub>2</sub> VCDs from mobile-car MAX-DOAS measurements performed by the  
364 Chinese Academy of Meteorological Sciences (CAMS) in the Three Rivers' Source region in July 2021  
365 (Cheng et al., 2023). The Three Rivers' Source region is on the northeastern Tibetan Plateau in western  
366 China, which is isolated from massive anthropogenic activities, and hence a good place for observations  
367 of atmospheric compositions in the background atmosphere. The field campaign lasted from 18<sup>th</sup> to 30<sup>th</sup>  
368 July 2021 and included four closed-loop journeys, beginning from the meteorological bureau of the city  
369 of Xining (the Capital of Qinghai Province) to the meteorological bureau of Dari County of the Guoluo  
370 Tibetan Autonomous Prefecture, to the meteorological bureau of Yushu Tibetan Autonomous Prefecture,  
371 and then back to Xining City (Figure S6). The spectral analysis of the measurement spectra in the fitting  
372 window of 400-434 nm was implemented with the DOAS method. Sequential Fraunhofer reference  
373 spectrum (FRS) is used to derive NO<sub>2</sub> differential slant column densities (DSCDs), which are then  
374 converted to VCDs by adopting the geometric approximation method. The errors are estimated to be less  
375 than 20% at high altitudes. More detailed descriptions of instrumentation, field campaign and data  
376 retrieval are in Cheng et al. (2023).

377 We average all valid mobile-car MAX-DOAS measurements within each observation period of  
378 GEMS in each  $0.05^\circ \times 0.05^\circ$  grid cell, to ensure spatiotemporal consistency. Over relatively clean areas  
379 with little human influence and biomass burning such as the Three Rivers' Source region, a large portion  
380 of NO<sub>2</sub> is located in the middle and upper troposphere, which is not accounted for in the mobile-car data

381 via such a DSCD-based retrieval method. Indeed, Cheng et al. (2023) showed that the official TROPOMI  
382 NO<sub>2</sub> VCDs are higher than mobile-car data by about 40%. Considering that the diurnal variation of  
383 middle and upper tropospheric NO<sub>2</sub> is much smaller than that in the lower troposphere, we focus on the  
384 correlation of NO<sub>2</sub> diurnal variation between POMINO-GEMS and mobile car MAX-DOAS data.

## 385 **2.5 Ground-based MEE NO<sub>2</sub> measurements**

386 We use hourly surface NO<sub>2</sub> mass concentration measurements from the MEE air quality monitoring  
387 network. By 2021, more than 2000 MEE stations across China have been established, providing hourly  
388 observations for NO<sub>2</sub> and five other air pollutants. Most stations are in urban or suburban areas.

389 The spatial distribution of all MEE sites in the GEMS FOV is shown in Figure S8a, and that of MEE  
390 sites over urban, suburban and rural regions are shown in Figure S8b–d, respectively. The classification  
391 of sites is based on Tencent user location data with a horizontal resolution of  $0.05^\circ \times 0.05^\circ$  for every 0.5  
392 second from 31 August to 30 September 2021 (Figure S8e), adopted from previous work (Kong et al.,  
393 2022a). Here, urban MEE sites are defined as where the mean location request times is larger than 50  
394 times per second, suburban sites refer to 5-50 times per second, and rural sites refer to less than 5 times  
395 per second. The number of sites for urban, suburban and rural sites are 808, 554 and 71, respectively.

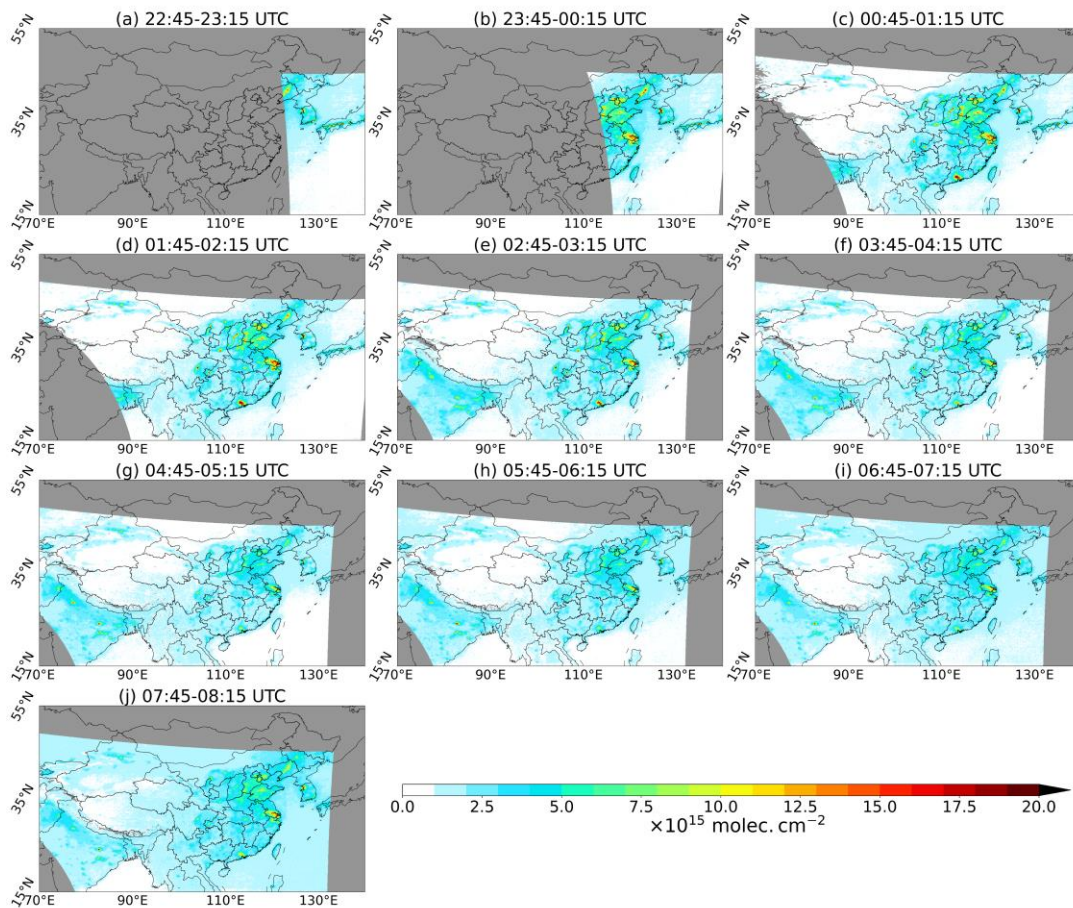
396 At MEE sites, molybdenum catalyzed conversion from NO<sub>2</sub> to NO and subsequent  
397 chemiluminescence measurement of NO is done to estimate NO<sub>2</sub> concentrations. The heated  
398 molybdenum catalyst has low chemical selectivity, leading to strong interference from other oxidized  
399 nitrogen species such as nitric acid (HNO<sub>3</sub>) and peroxyacetyl nitrate (PAN). Therefore, MEE data tend  
400 to overestimate the actual NO<sub>2</sub> concentrations, with the extent of overestimation about 10% – 50%  
401 (Boersma et al., 2009; Liu et al., 2018a). The overestimation is dependent on the oxidation level of NO<sub>x</sub>,  
402 but is currently unclear for each site and hour.

403 To compare with satellite-derived surface NO<sub>2</sub> concentration data, we average over all valid MEE  
404 sites in each  $0.05^\circ \times 0.05^\circ$  grid cell to generate gridded MEE NO<sub>2</sub> data for each hour. To ensure sampling  
405 consistency for each day, we average MEE observations at two consecutive hours to match GEMS hourly  
406 observations – for example, we match the mean value of MEE NO<sub>2</sub> concentrations in 13:00 – 14:00 and  
407 14:00 – 15:00 local solar time (LST) with the GEMS NO<sub>2</sub> in 13:45 – 14:15 LST. We also match MEE  
408 observations over the period 13:00 – 14:00 LST with TROPOMI-derived and OMI-derived surface NO<sub>2</sub>,  
409 and 9:00 – 10:00 LST with GOME-2-derived surface NO<sub>2</sub>.

410 **3. Results and discussion**

411 **3.1 POMINO-GEMS tropospheric NO<sub>2</sub> VCDs**

412 Figure 4 shows mean POMINO-GEMS tropospheric NO<sub>2</sub> VCDs at each hour on a 0.05° × 0.05°  
413 grid in JJA 2021. High values of tropospheric NO<sub>2</sub> columns (> 10 × 10<sup>15</sup> molec. cm<sup>-2</sup>) are evident over  
414 populous regions such as South Korea, central and eastern China, and northern India. Clear hotspot  
415 signals reveal intense NO<sub>x</sub> emissions over city clusters such as Beijing-Tianjin-Hebei (BTH), Yangtze  
416 River Delta (YRD), Pearl River Delta (PRD) and Seoul Metropolitan Area (SMA), as well as isolated  
417 megacities such as Osaka and Nagoya in Japan, Chengdu and Urumqi in China, and New Delhi in India.  
418 Tropospheric NO<sub>2</sub> VCDs are much lower (< 1 × 10<sup>15</sup> molec. cm<sup>-2</sup>) over most of western China and the  
419 open ocean, due to low anthropogenic and natural emissions.

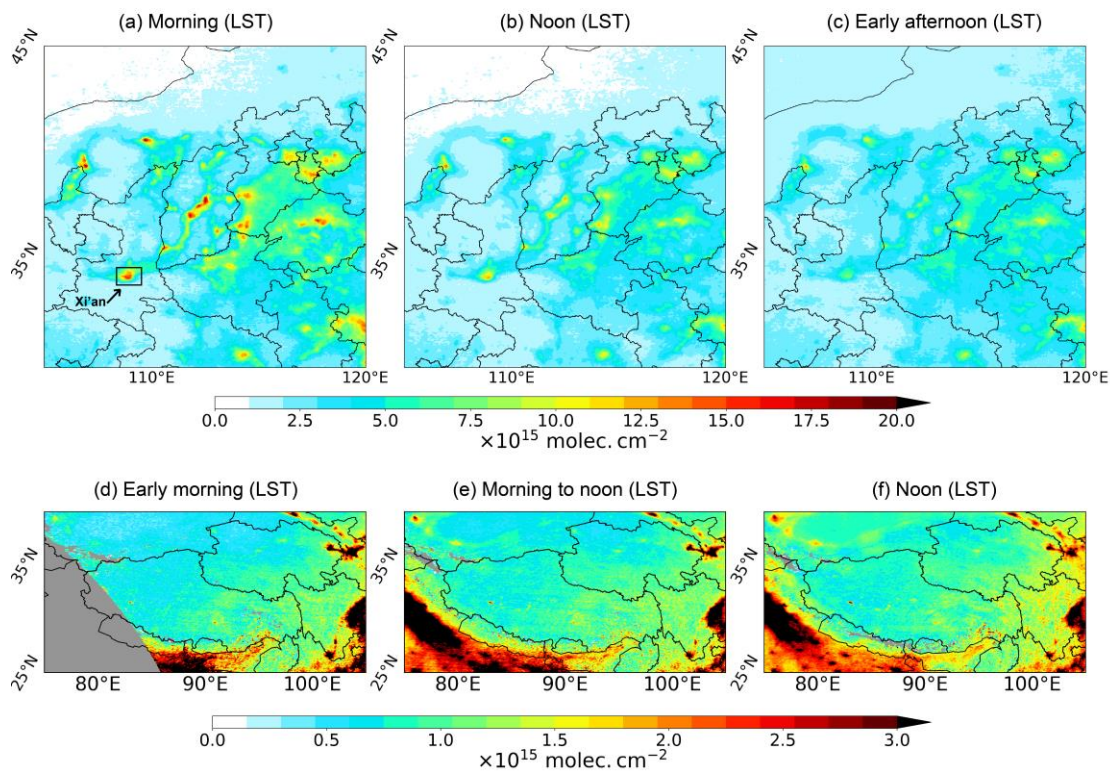


420  
421 **Figure 4. Spatial distribution of POMINO-GEMS tropospheric NO<sub>2</sub> VCDs at each hour on a 0.05° × 0.05°**  
422 **grid in JJA 2021. The regions in grey mean there are no valid observations.**

423 Figure 5a-c present NO<sub>2</sub> VCDs in the morning, noon and afternoon in JJA 2021 for eastern China.  
424 Data are averaged in 22:45 – 01:45 UTC (06:45 – 09:45 Beijing Time, BJT), 02:45 – 04:45 UTC (10:45



425 – 12:45 BJT) and 05:45 – 07:45 UTC (13:45 – 15:45 BJT) to represent the morning, noon and afternoon,  
 426 respectively. In the morning (Figure 5a), there are clear city signals with high  $\text{NO}_2$  values, reflecting  
 427 abundant  $\text{NO}_x$  emissions from traffic. The spatial gradients of  $\text{NO}_2$  from urban centers to outskirts are  
 428 very strong. However, these spatial gradients are greatly reduced in the noon and afternoon (Figure 5b  
 429 and c). For example, the differences of tropospheric  $\text{NO}_2$  VCDs between the urban center of Xi'an  
 430 ( $108.93^\circ\text{N}$ ,  $34.27^\circ\text{E}$ ) and its surrounding areas (within 50 km) are reduced from about  $8 \times 10^{15}$  molec.  
 431  $\text{cm}^{-2}$  in the morning to about  $4 \times 10^{15}$  molec.  $\text{cm}^{-2}$  at noon, and then to below  $2 \times 10^{15}$  molec.  $\text{cm}^{-2}$  in the  
 432 afternoon. This is likely due to chemical loss of traffic-associated  $\text{NO}_2$ , increased emissions from other  
 433 sectors (e.g., industry), and/or enhanced horizontal transport smearing the spatial gradient.



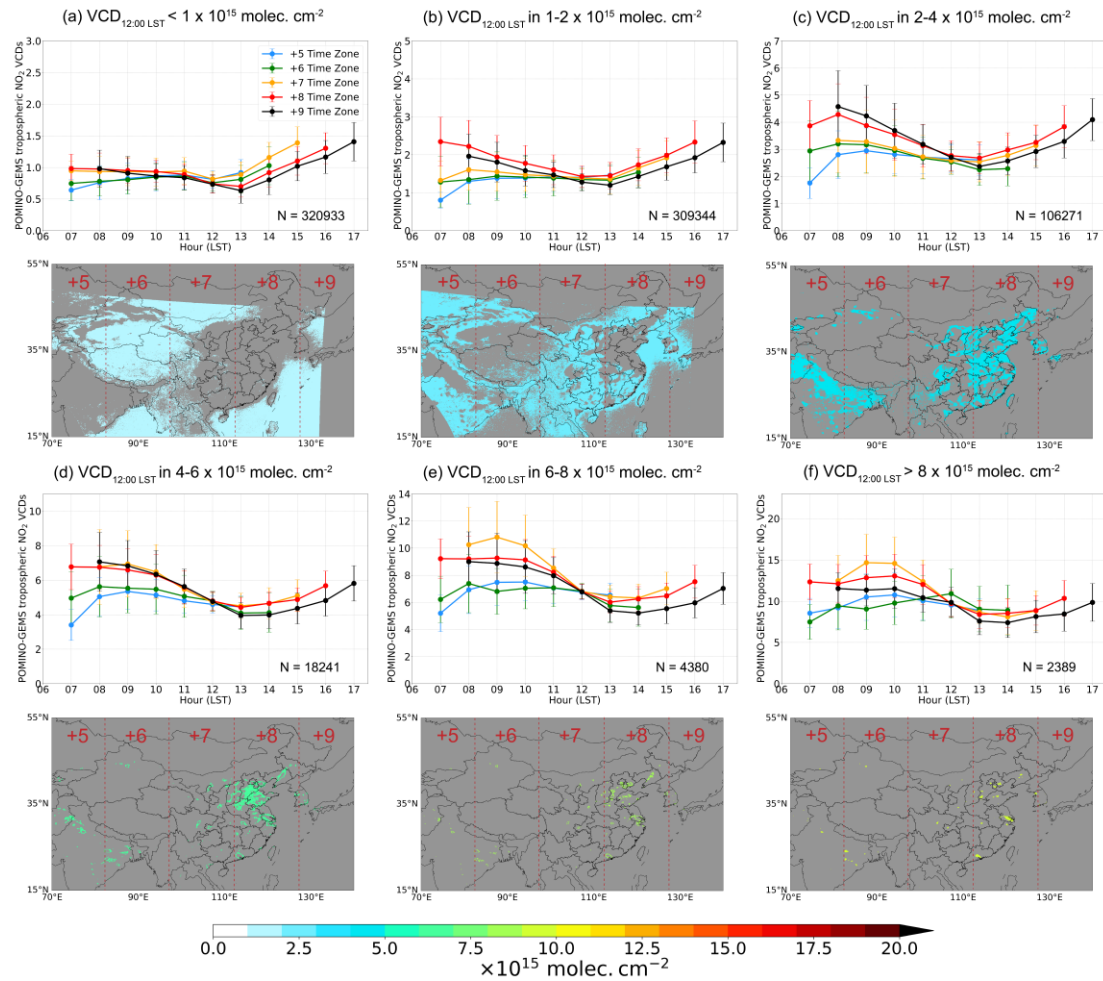
434  
 435 **Figure 5. Spatial distribution of three-hour-mean POMINO-GEMS tropospheric  $\text{NO}_2$  VCDs in JJA 2021 on**  
 436 **a  $0.05^\circ \times 0.05^\circ$  grid. The first row is for eastern China in the (a) morning (22:45 – 01:45 UTC), (b) noon**  
 437 **(02:45 – 04:45 UTC) and (c) afternoon (05:45 – 07:45 UTC). The second row is for western China in the (d)**  
 438 **early morning (00:45 – 01:45 UTC), (e) morning to noon (02:45 – 04:45 UTC) and (f) noon (05:45 – 07:45**  
 439 **UTC). The regions in grey mean there are no valid observations.**

440 Over western China with low tropospheric  $\text{NO}_2$  VCDs (Figure 5d-f), there is a gradual increase of  
 441 tropospheric  $\text{NO}_2$  by about  $1 \times 10^{15}$  molec.  $\text{cm}^{-2}$  from the early morning to noon. This increase is likely  
 442 dominated by biogenic  $\text{NO}_x$  emissions that are sensitive to sunshine intensity and surface temperature  
 443 (Kong et al., 2022b; Weng et al., 2020; Kong et al., 2023). Future studies are needed to understand the

444 exact causes.

445 Figure 6 shows the diurnal variation of POMINO-GEMS tropospheric NO<sub>2</sub> VCDs over six different  
446 region groups in the GEMS FOV. The six groups are defined based on the levels of mean POMINO-  
447 GEMS tropospheric NO<sub>2</sub> VCDs at 12:00 LST in JJA 2021 ( $VCD_{12:00\text{ LST}}$ ), and their spatial distributions  
448 are also shown in each panel. We convert the observation time from UTC to LST for each time zone in  
449 this domain (+5 time zone: 70°E – 82.5° E; +6 time zone: 82.5°E – 97.5°E; +7 time zone: 97.5°E –  
450 112.5°E; +8 time zone: 112.5°E – 127.5°E; +9 time zone: 127.5°E – 140°E), and show the NO<sub>2</sub> diurnal  
451 variations in each time zone with different colors. For low NO<sub>2</sub> situations ( $VCD_{12:00\text{ LST}} \leq 2 \times 10^{15}$  molec.  
452 cm<sup>-2</sup>), NO<sub>2</sub> grow in the morning time in +5 and +6 time zones but not in other time zones. Over high  
453 NO<sub>2</sub> situations ( $VCD_{12:00\text{ LST}} > 8 \times 10^{15}$  molec. cm<sup>-2</sup>, in cities and suburban areas), NO<sub>2</sub> in all time zones  
454 exhibit a minimum around noontime and a morning peak at 09:00 – 10:00 LST, consistent with previous  
455 findings for specific polluted locations (Boersma et al., 2008; Boersma et al., 2009; Li et al., 2021a;  
456 Ghude et al., 2020; Herman et al., 2019; Biswas and Mahajan, 2021). In all groups and time zones,  
457 tropospheric NO<sub>2</sub> VCDs grow from noon to the afternoon.

458 The NO<sub>2</sub> diurnal variations are related to multiple driving factors. Different sources with distinctive  
459 diurnal patterns dominate the NO<sub>x</sub> emissions over different regions. Lightning and biogenic activities are  
460 the major emission sources over low NO<sub>2</sub> land areas, and they tend to intensify with temperature and  
461 radiation in the daytime. Anthropogenic emissions are dominant over polluted cities and suburban areas,  
462 where the traffic emissions tend to peak in the mid-morning and late afternoon (Jing et al., 2016; Liu et  
463 al., 2018b; Naiudomthum et al., 2022). In addition, the photochemistry plays an important role. NO<sub>2</sub> is  
464 in chemical balance with NO, and the ratio of NO<sub>2</sub> and NO depends on radiation, ozone and peroxy  
465 radicals. NO<sub>x</sub> is oxidized to nitric acid and organic nitrates by radicals in the daytime, the level of which  
466 depends on radiation, ozone and volatile organic compounds. Thus the lifetime of NO<sub>2</sub> reaches the  
467 minimum value around noon, i.e., a few hours in summer. Furthermore, atmospheric transport also affects  
468 the diurnal variation of NO<sub>2</sub> at high-value places (e.g., cities) and their surroundings. Further studies are  
469 needed to determine the exact causes of NO<sub>2</sub> diurnal variations at individual places.



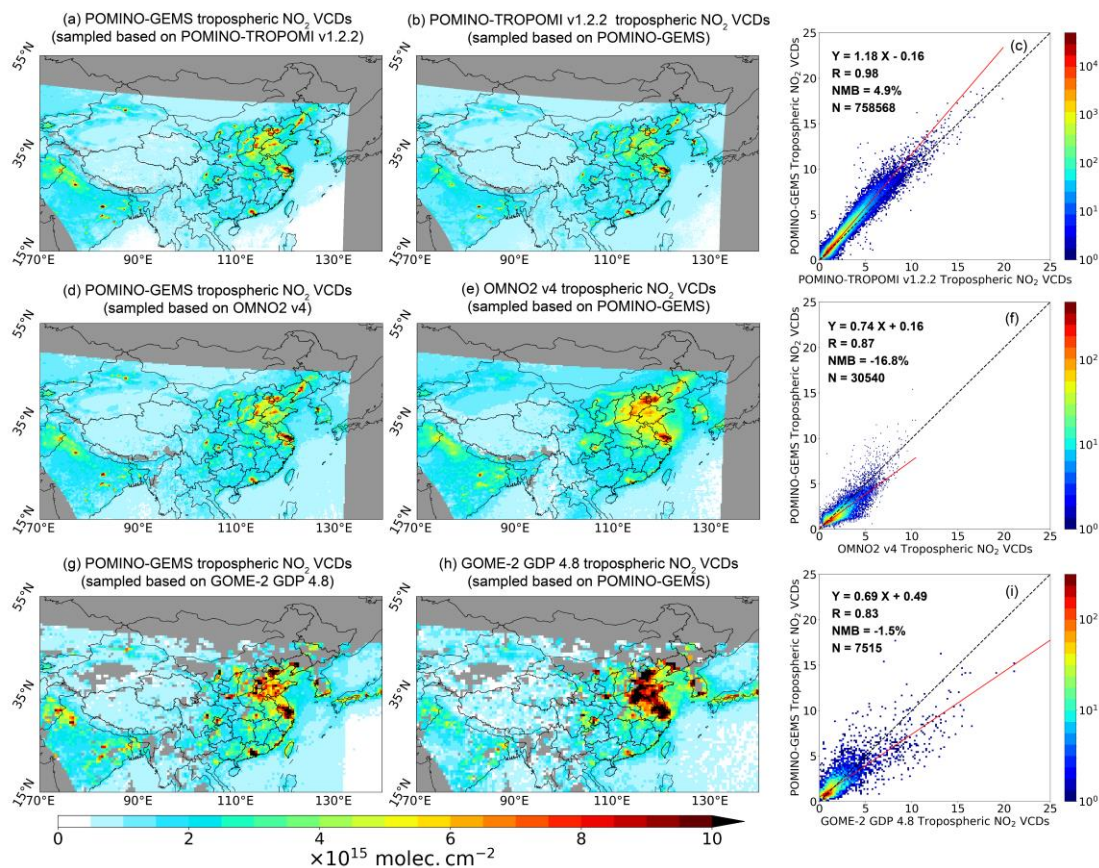
470

471 **Figure 6. POMINO-GEMS NO<sub>2</sub> diurnal variations for six region groups classified based on mean**  
 472 **POMINO-GEMS tropospheric NO<sub>2</sub> VCDs at 12:00 LST in JJA 2021 (VCD<sub>12:00 LST</sub>). (a) VCD<sub>12:00 LST</sub> less than**  
 473 **1 × 10<sup>15</sup> molec. cm<sup>-2</sup>; (b) VCD<sub>12:00 LST</sub> in 1 – 2 × 10<sup>15</sup> molec. cm<sup>-2</sup>; (c) VCD<sub>12:00 LST</sub> in 2 – 4 × 10<sup>15</sup> molec. cm<sup>-2</sup>;**  
 474 **(d) VCD<sub>12:00 LST</sub> in 4 – 6 × 10<sup>15</sup> molec. cm<sup>-2</sup>; (e) VCD<sub>12:00 LST</sub> in 6 – 8 × 10<sup>15</sup> molec. cm<sup>-2</sup> and (f) VCD<sub>12:00 LST</sub>**  
 475 **larger than 8 × 10<sup>15</sup> molec. cm<sup>-2</sup>. In each panel, different colors denote the NO<sub>2</sub> diurnal variation in different**  
 476 **time zones. N denotes the total number of valid 0.05° × 0.05° grid cells in each region. The error bars denote**  
 477 **the standard deviation of tropospheric NO<sub>2</sub> VCDs at each hour in each time zone.**

478 **3.2 Comparison with POMINO-TROPOMI v1.2.2, OMNO2 v4 and GOME-2 GDP 4.8 NO<sub>2</sub> VCD**  
 479 **products**

480 Figure 7a and b show the POMINO-GEMS and POMINO-TROPOMI v1.2.2 tropospheric NO<sub>2</sub>  
 481 VCDs, respectively, on a 0.05° × 0.05° grid averaged over JJA 2021. Cloud screening is implemented  
 482 based on the CRFs from each product. To ensure temporal compatibility, matching between hourly  
 483 GEMS observations and the TROPOMI data at the closest observation time is done for each day. Overall,  
 484 POMINO-GEMS agrees well with POMINO-TROPOMI with a spatial correlation coefficient of 0.98, a  
 485 linear regression slope of 1.18 and a small positive NMB of 4.9% (Figure 7c). Regionally, POMINO-

486 GEMS VCDs are higher than those of POMINO-TROPOMI v1.2.2 over eastern China, most India and  
 487 northwestern GEMS FOV, but smaller over western China and the oceans (Figure 7a, b; see Figure S9c  
 488 and d for differences plots). These differences are related to tropospheric NO<sub>2</sub> AMFs and SCDs. Detailed  
 489 discussion is given in Section 3 of the SI.



490  
 491 **Figure 7. Comparison between POMINO-GEMS and other products for tropospheric NO<sub>2</sub> VCDs in JJA**  
 492 **2021. (a-b) Between POMINO-GEMS and POMINO-TROPOMI v1.2.2 on a  $0.05^\circ \times 0.05^\circ$  grid, (d-e)**  
 493 **between POMINO-GEMS and OMNO2 v4 on a  $0.25^\circ \times 0.25^\circ$  grid, and (g-h) between POMINO-GEMS and**  
 494 **GOME-2 GDP 4.8 on a  $0.5^\circ \times 0.5^\circ$  grid. (c), (f) and (i) are respective scatterplots, in which the colors**  
 495 **represent data density. The regions in grey mean there are no valid observations.**

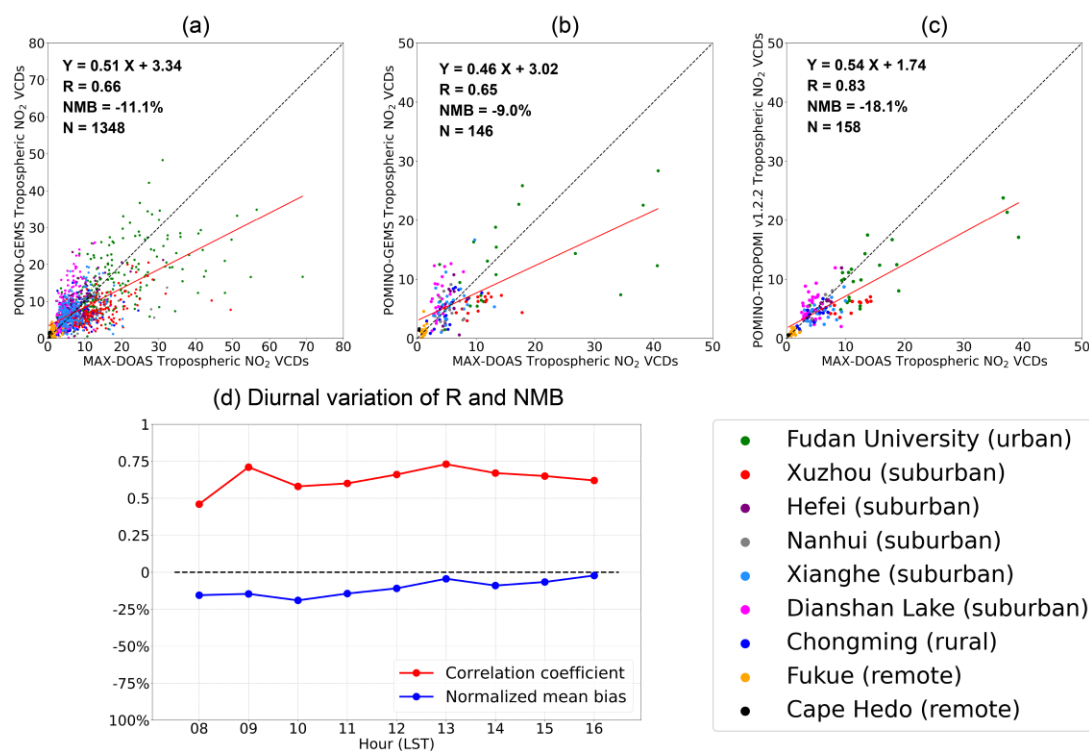
496 Figure 7d-f and g-i show the comparison results of POMINO-GEMS tropospheric NO<sub>2</sub> VCDs with  
 497 OMNO2 v4 on a  $0.25^\circ \times 0.25^\circ$  grid and GOME-2 GDP 4.8 on a  $0.5^\circ \times 0.5^\circ$  grid averaged over JJA 2021,  
 498 respectively. POMINO-GEMS NO<sub>2</sub> VCDs exhibit good spatial consistency with the two independent  
 499 products ( $R = 0.87$  and  $0.83$ ), although with slightly lower values than OMNO2 v4 (by 16.8%) and  
 500 GOME-2 GDP 4.8 (by 1.5%). These VCD differences are expected, considering the differences in the  
 501 retrieval algorithm. For example, the POMINO-GEMS algorithm implements explicit aerosol  
 502 corrections in the radiative transfer calculation, while OMNO2 v4 and GOME-2 GDP 4.8 treat aerosols  
 503 as “effective clouds”. POMINO-GEMS accounts for the anisotropy of surface reflectance by adopting

504 MODIS BRDF coefficients, whereas OMNO2 v4 and GOME-2 GDP 4.8 use geometry-dependent and  
 505 regular LER, respectively. The horizontal resolution of a priori NO<sub>2</sub> profiles in POMINO-GEMS is 25  
 506 km (and interpolated to 2.5 km), 1° × 1.25° in OMNO2 v4 and 1.875° × 1.875° in GOME-2 GDP 4.8  
 507 (Valks, 2019; Lamsal et al., 2021).

508 Based on comparisons with POMINO-TROPOMI v1.2.2, OMNO2 v4 and GOME-2 GDP 4.8 NO<sub>2</sub>  
 509 VCDs, we conclude that POMINO-GEMS NO<sub>2</sub> columns show good agreement with LEO satellite data,  
 510 with lower values by 20% at most.

### 511 3.3 Validation with MAX-DOAS NO<sub>2</sub> VCD measurements

512 The scatterplot in Figure 8a compares POMINO-GEMS tropospheric NO<sub>2</sub> VCDs in JJA 2021 at all  
 513 GEMS observation hours with matched ground based MAX-DOAS measurements at nine sites.  
 514 POMINO-GEMS correlates with MAX-DOAS ( $R = 0.66$ ) with a small negative bias (NMB = -11.1%).  
 515 The linear regression shows a slope of 0.51 and intercept of  $3.34 \times 10^{15}$  molec. cm<sup>-2</sup>, reflecting  
 516 underestimation of POMINO-GEMS tropospheric NO<sub>2</sub> VCDs on high-NO<sub>2</sub> days.



517  
 518 **Figure 8. Evaluation of satellite NO<sub>2</sub> VCD data using ground-based MAX-DOAS measurements. (a)**  
 519 **Scatterplot for tropospheric NO<sub>2</sub> VCDs ( $\times 10^{15}$  molec. cm<sup>-2</sup>) between MAX-DOAS and POMINO-GEMS at**  
 520 **all GEMS observation hours in JJA 2021. Each data pair denotes an hour. (b-c) Scatterplots for**  
 521 **tropospheric NO<sub>2</sub> VCDs ( $\times 10^{15}$  molec. cm<sup>-2</sup>) in JJA 2021 (b) between MAX-DOAS and POMINO-GEMS at**  
 522 **13:45 – 14:15 LST and (c) between MAX-DOAS and POMINO-TROPOMI v1.2.2. Each data pair denotes a**  
 523 **day. Each MAX-DOAS station is color-coded. (d) Diurnal variations of spatiotemporal correlation**

524 **coefficients and NMBs of POMINO-GEMS tropospheric NO<sub>2</sub> VCDs relative to ground-based MAX-DOAS**  
525 **data.**

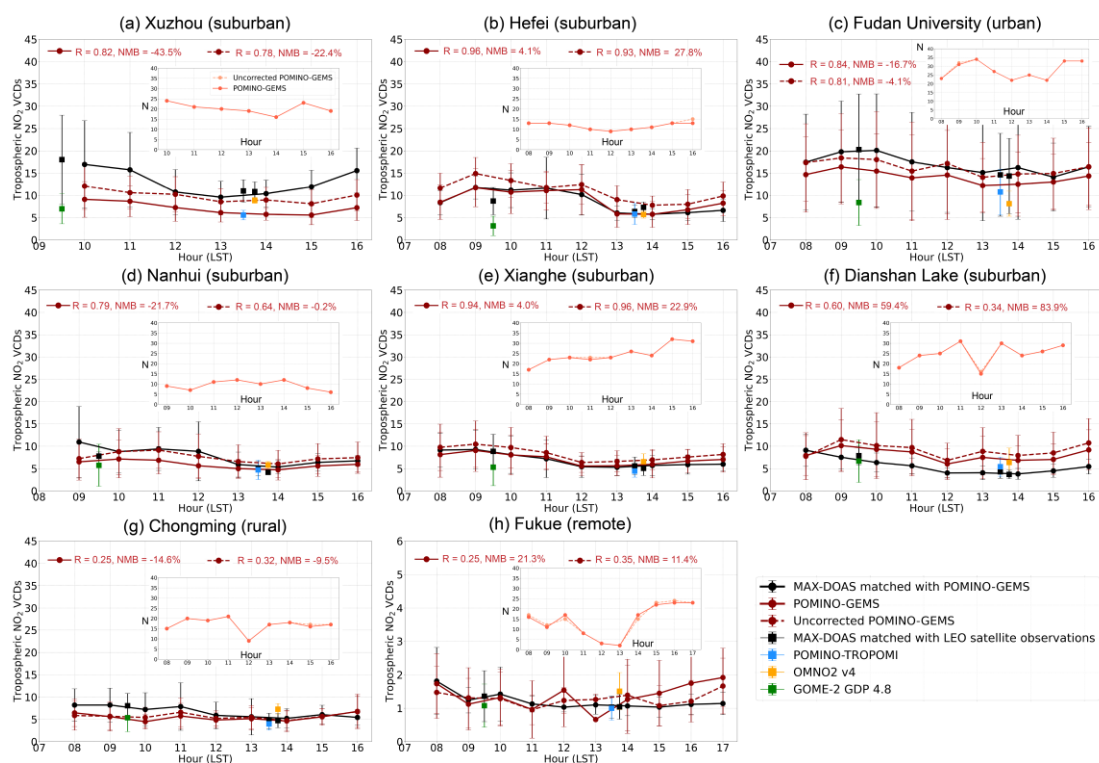
526 Figure 8b-c further use MAX-DOAS measurements to evaluate POMINO-GEMS and POMINO-  
527 TROPOMI v1.2.2 tropospheric NO<sub>2</sub> VCDs at the overpass time of TROPOMI. In Figure 8b, POMINO-  
528 GEMS data at 13:45 – 14:15 LST are used to match the overpass time of TROPOMI. The POMINO-  
529 TROPOMI product is evaluated in the context of understanding the relative performance of POMINO-  
530 GEMS. Each data point represents a day. Figure 8b-c show that the day-to-day variability of MAX-  
531 DOAS measurements is well captured by POMINO-TROPOMI v1.2.2 ( $R = 0.83$ ), but less so by  
532 POMINO-GEMS ( $R = 0.65$ ). Linear regression results show an underestimate of tropospheric NO<sub>2</sub> VCDs  
533 in POMINO-TROPOMI v1.2.2 (NMB = -18.1%), as also found in previous studies (Liu et al., 2020).  
534 POMINO-GEMS exhibits a small bias (NMB = -9.0%), but station-dependent performance is apparent.  
535 At the two remote sites of Fukue and Cape Hedo with low NO<sub>2</sub>, POMINO-GEMS NO<sub>2</sub> columns are  
536 higher than those of MAX-DOAS measurements. At the other sites, the data pairs are more scattered and  
537 located both above and below the 1:1 line, resulting in a small NMB.

538 Figure 8d shows the NMBs and correlation coefficients of POMINO-GEMS NO<sub>2</sub> VCDs relative to  
539 ground-based MAX-DOAS data at each hour. The negative NMBs reach a maximum of about 20% at  
540 10:00 BJT, and decrease to less than 10% in the afternoon. The correlation coefficients are modest or  
541 high (0.45 – 0.73) at all hours.

542 Figure 9 compares the diurnal variation of tropospheric NO<sub>2</sub> VCDs between POMINO-GEMS and  
543 MAX-DOAS at eight stations. At each site, NO<sub>2</sub> values are averaged in JJA 2021 at each hour for  
544 comparison, and the number of valid days for each hour is also shown. The Cape Hedo site is not included  
545 because there are few valid MAX-DOAS data points at each hour. Figure 10a-f show that at the urban  
546 and suburban sites, MAX-DOAS NO<sub>2</sub> (black lines) peaks in the mid-to-late morning, declines towards  
547 the minimum values at noon around 13:00 LST, and then gradually increases in the afternoon. Strong  
548 correlation of NO<sub>2</sub> diurnal variation between POMINO-GEMS (red solid lines) and MAX-DOAS is  
549 found at Xuzhou ( $R = 0.82$ ), Hefei ( $R = 0.96$ ), Fudan University ( $R = 0.84$ ), Nanhui ( $R = 0.79$ ) and  
550 Xianghe ( $R = 0.94$ ). At the Dianshan Lake site, POMINO-GEMS NO<sub>2</sub> columns increase but MAX-  
551 DOAS data decrease from 08:00 to 09:00 LST, resulting in a lower correlation coefficient ( $R = 0.60$ ). At  
552 Chongming and Fukue sites, MAX-DOAS NO<sub>2</sub> shows a peak in the morning without evident increase in  
553 the early afternoon, but this diurnal pattern is not fully captured by POMINO-GEMS. At Fukue,

554 POMINO-GEMS NO<sub>2</sub> exhibit abrupt changes at 12:00 and 13:00 LST due to few valid data.

555 In addition, comparison of POMINO-GEMS diurnal variation with NO<sub>2</sub> data from GOME-2 in the  
 556 morning and OMI and TROPOMI in the early afternoon shows good agreement at Hefei, Nanhui,  
 557 Dianshan Lake, Chongming and Fukue sites. The differences between POMINO-GEMS to MAX-DOAS  
 558 NO<sub>2</sub> VCDs are comparable or smaller than those between LEO satellite and MAX-DOAS NO<sub>2</sub> VCDs.



559

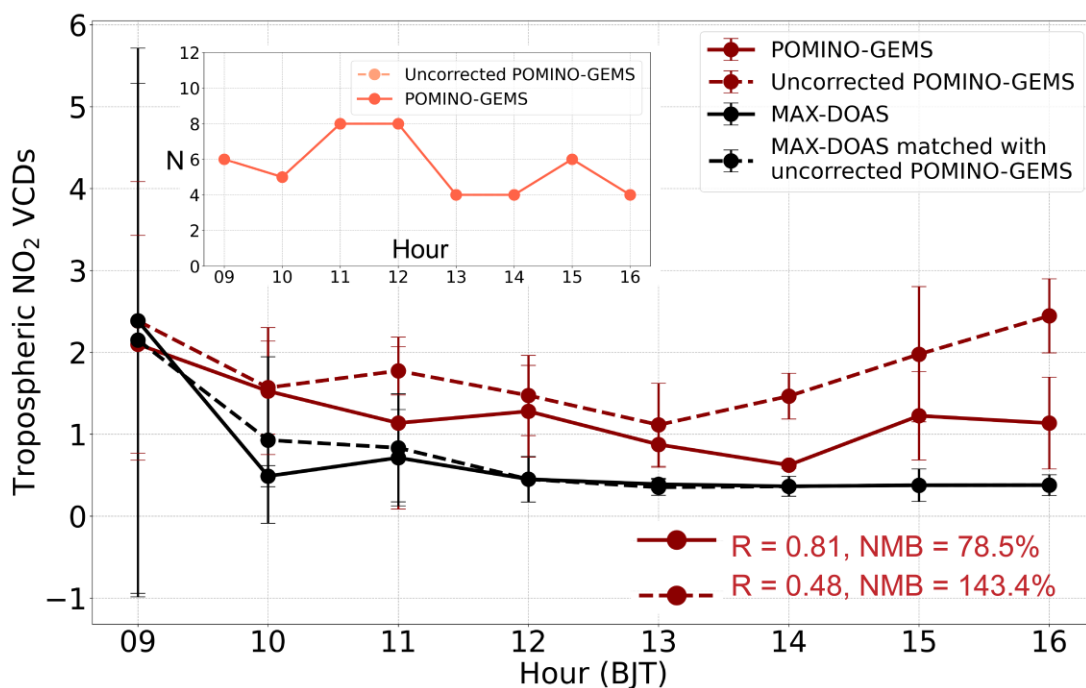
560 **Figure 9.** Diurnal variation of hourly tropospheric NO<sub>2</sub> VCDs ( $\times 10^{15}$  molec. cm<sup>-2</sup>) of MAX-DOAS (black  
 561 lines), and POMINO-GEMS with TROPOMI correction (red solid lines), and re-calculated POMINO-  
 562 GEMS without TROPOMI correction (red dashed lines) at eight sites in JJA 2021. The error bars denote  
 563 the standard deviation of MAX-DOAS and POMINO-GEMS NO<sub>2</sub> at each hour, respectively. Diurnal  
 564 correlation and all-hour-mean NMB of POMINO-GEMS against MAX-DOAS data are shown. The number  
 565 of valid days for each hour is also presented. The black squares with an error bar represent the mean value  
 566 and standard deviation of MAX-DOAS tropospheric NO<sub>2</sub> VCDs matched with POMINO-TROPOMI v1.2.2  
 567 (blue squares), OMNO2 v4 (orange squares) and GOME-2 GDP 4.8 (green squares), respectively.

568 As we use TROPOMI total NO<sub>2</sub> SCDs to correct those of GEMS, this may influence the NO<sub>2</sub> diurnal  
 569 variation of original GEMS observations. Thus we also compare MAX-DOAS data with re-calculated  
 570 POMINO-GEMS tropospheric NO<sub>2</sub> VCDs without correction in total SCDs (red dashed lines in Figure  
 571 9). Compared to our default POMINO-GEMS data (with correction), excluding the correction leads to  
 572 lower diurnal correlation coefficients at Xuzhou, Hefei, Fudan University, Nanhui and Dianshan Lake,  
 573 but higher correlation coefficients at Xianghe, Chongming and Fukue. Excluding the correction increases

574 the NMB at three sites but decreases the NMB at five sites. We conclude that at these eight sites (in the  
 575 eastern areas), no significant influence on the diurnal variation of POMINO-GEMS tropospheric NO<sub>2</sub>  
 576 VCDs is brought in through TROPOMI-based correction for total NO<sub>2</sub> SCDs.

577 Figure 10 compares the diurnal variations between POMINO-GEMS and mobile-car MAX-DOAS  
 578 tropospheric NO<sub>2</sub> VCD data in the Three Rivers' Source region on the Tibetan Plateau. Results of  
 579 POMINO-GEMS with and without total SCD correction are shown in the red solid and dashed lines,  
 580 respectively. Mobile-car MAX-DOAS data show an evident decrease of tropospheric NO<sub>2</sub> VCDs from  
 581 the morning to noon with little change thereafter. Such NO<sub>2</sub> diurnal patterns reflect the spatial and  
 582 temporal variations of tropospheric NO<sub>2</sub> along the driving route. The high NO<sub>2</sub> values with large standard  
 583 deviation at 09:00 BJT is due to enhanced pollution and variability in the morning when the car is in or  
 584 near the Xining city. The NO<sub>2</sub> diurnal variations of POMINO-GEMS with correction correlate well with  
 585 those of mobile-car MAX-DOAS data ( $R = 0.81$ ). In contrast, POMINO-GEMS without total SCD  
 586 correction exhibits much poorer correlation with mobile-car MAX-DOAS data, due to the erroneous  
 587 increase in the afternoon.

588 Overall, the validation results with independent ground-based and mobile-car MAX-DOAS  
 589 measurements provide confidence on the general characteristics of POMINO-GEMS NO<sub>2</sub> diurnal  
 590 variations.



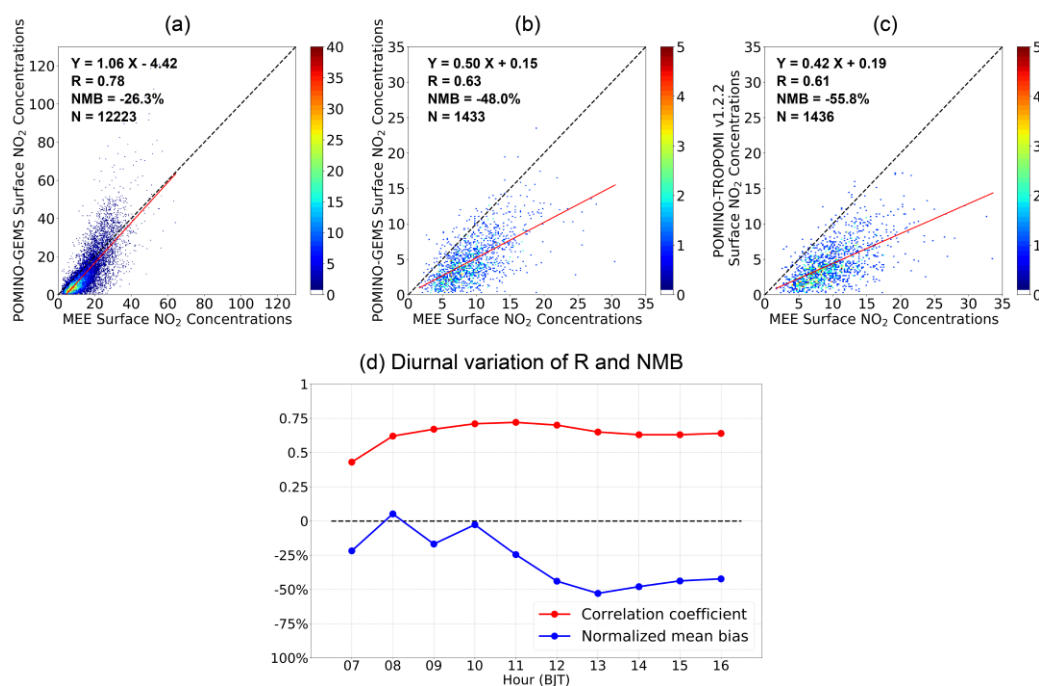
591  
 592 **Figure 10. Diurnal variation of hourly mean tropospheric NO<sub>2</sub> VCDs ( $\times 10^{15}$  molec. cm<sup>-2</sup>) of mobile-car**  
 593 **MAX-DOAS and POMINO-GEMS in the Three Rivers' Source region. The black solid lines denote MAX-**



594 DOAS data that spatiotemporally match with POMINO-GEMS with total SCD correction (red solid lines).  
 595 The black dashed lines denote MAX-DOAS data that spatiotemporally match with POMINO-GEMS  
 596 without correction (red dashed lines). The error bars denote the standard deviation of MAX-DOAS and  
 597 POMINO-GEMS NO<sub>2</sub> at each hour during the field campaign, respectively. Values for diurnal correlation  
 598 and mean NMB of POMINO-GEMS relative to MAX-DOAS are shown. The number of days with valid  
 599 data for each hour is also presented.

### 600 3.4 Validation with surface NO<sub>2</sub> concentration measurements from MEE

601 The scatterplot in Figure 11a compares surface NO<sub>2</sub> concentrations derived from POMINO-GEMS  
 602 with MEE measurements at all hours. POMINO-GEMS derived surface NO<sub>2</sub> concentrations show good  
 603 agreement with MEE measurements in terms of spatiotemporal correlation ( $R = 0.78$ ) and bias (NMB =  
 604  $-26.3\%$ ), but are higher than those of MEE at some high-value situations, which mainly occur over the  
 605 YRD region (Figure S14). These differences reflect errors in POMINO-GEMS NO<sub>2</sub> VCDs, in the  
 606 conversion from tropospheric VCDs to surface concentrations, and in MEE data (due to potential  
 607 contamination by nitric acid and organic nitrates (Liu et al., 2018a)).



608  
 609 **Figure 11. Evaluation of satellite-derived surface NO<sub>2</sub> concentrations ( $\mu\text{g m}^{-3}$ ) using MEE measurements in**  
 610 **JJA 2021. (a) Scatterplot for MEE and POMINO-GEMS at all GEMS observation hours averaged over all**  
 611 **days in JJA 2021. (b) Scatterplot for MEE and POMINO-GEMS at 13:45 – 14:15 LST. (c) Scatterplot for**  
 612 **MEE and POMINO-TROPOMI v1.2.2. The color bar represents the data density. (d) Diurnal variations of**  
 613 **spatiotemporal correlation coefficients and NMBs of POMINO-GEMS derived surface NO<sub>2</sub> concentrations**  
 614 **relative to MEE measurements.**

615 Figure 11b-c show validation results for satellite-derived surface NO<sub>2</sub> concentrations with MEE

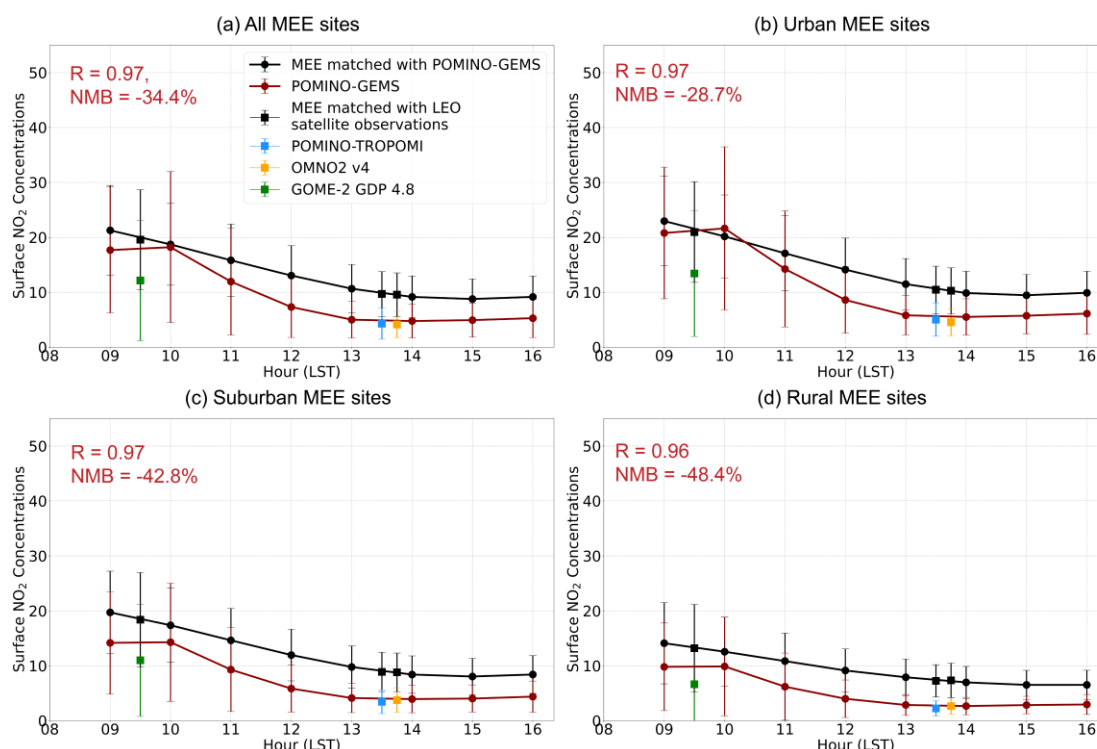
616 measurements at the overpass time of TROPOMI (i.e., early afternoon). Here, each data pair denotes a  
617 MEE site. POMINO-GEMS results at 13:45 – 14:15 LST are used to match the overpass time of  
618 TROPOMI data. Overall, both satellite-based datasets show good spatial correlation with MEE  
619 measurements ( $R = 0.63$  and  $0.61$ ). POMINO-GEMS exhibits higher linear regression slope ( $0.50$ ) with  
620 smaller NMB ( $-48.0\%$ ). The values of satellite data are lower than those from MEE, especially in the  
621 afternoon (Figure 11d). This is in part because of the aforementioned contamination issues in MEE data,  
622 which becomes severer in the afternoon as the air gets more aged throughout the daytime.

623 Figure 12a examines the diurnal variation of surface  $\text{NO}_2$  concentrations averaged over JJA 2021 at  
624 all sites. The MEE data show a smooth and monotonic decline from the early morning to the early  
625 afternoon, with a slight increase beginning at 15:00 LST. This diurnal pattern differs from those seen in  
626 ground-based MAX-DOAS VCD data (Figure 9), due to the difference in sampling size between MEE  
627 and MAX-DOAS, the diurnal variation of  $\text{NO}_2$  vertical distribution that affects the relationship between  
628 surface and columnar  $\text{NO}_2$ , as well as the insensitivity of  $\text{NO}_2$  columns to changes in PBL heights.  
629 POMINO-GEMS derived surface  $\text{NO}_2$  concentrations show similar diurnal variations to those of MEE  
630 ( $R = 0.97$ ), although with a peak at 10:00 LST and a gradual increase beginning at 14:00 LST. The  
631 discrepancies between POMINO-GEMS and MEE surface  $\text{NO}_2$  concentrations at different hours are  
632 likely caused by the assumed constant correction factor of 2 to account for the vertical gradient of  $\text{NO}_2$   
633 from the height of ground instrument to the center of the first model layer (Section 2.2). In the morning  
634 when the PBL is low, most  $\text{NO}_2$  molecules are near the ground and the vertical gradient of  $\text{NO}_2$  over  
635 polluted regions is the largest in the daytime, so the factor of 2 may lead to underestimation of derived  
636 surface  $\text{NO}_2$  concentrations. In contrast, in the afternoon, the PBL mixing is much stronger and the  
637 vertical gradient of  $\text{NO}_2$  is much smaller, thus the factor of 2 may lead to overestimated surface  $\text{NO}_2$   
638 concentrations. Note that the consistency between POMINO-GEMS and MEE data does not depend on  
639 the total SCD correction (Table S4).

640 To quantify the influences of the diurnal variation of hourly column-to-surface ratio from GEOS-  
641 Chem simulations, we compare the MEE measurements with POMINO-GEMS derived surface  $\text{NO}_2$   
642 concentrations using daily column-to-surface ratio (Figure S15). As expected, POMINO-GEMS derived  
643  $\text{NO}_2$  concentrations show a similar diurnal variation as the tropospheric  $\text{NO}_2$  VCDs do, with two peaks  
644 in the mid-morning and afternoon, and a minimum at noon. The temporal correlation coefficient with

645 MEE is only about 0.23. Thus it is more reasonable to use hourly ratio for comparison with MEE  
 646 measurements, as done in our study.

647 To further test the reliability of our VCD-to-surface-concentration conversion method (Eq. (9)), we  
 648 apply the same method to MAX-DOAS NO<sub>2</sub> VCDs and compare the resulting surface NO<sub>2</sub>  
 649 concentrations with MEE data. As shown in Figure S16, the diurnal variation of MAX-DOAS derived  
 650 surface NO<sub>2</sub> concentrations correlates well with that of MEE measurements ( $R = 0.96$ ), in support of our  
 651 conversion method.



652  
 653 **Figure 12. Diurnal variation of hourly surface NO<sub>2</sub> concentrations ( $\mu\text{g m}^{-3}$ ) of MEE (back lines) and**  
 654 **POMINO-GEMS (red lines) in JJA 2021. (a) At all MEE sites, (b) at urban sites, (c) at suburban sites and**  
 655 **(d) at rural sites. The error bars denote the standard deviation of MEE and POMINO-GEMS derived**  
 656 **surface NO<sub>2</sub> concentrations at each hour in JJA 2021, respectively. Diurnal correlation and mean NMB of**  
 657 **POMINO-GEMS relative to MEE are also listed. The black squares with an error bar represent the mean**  
 658 **value and standard deviation of MEE data matched with POMINO-TROPOMI v1.2.2 (blue squares),**  
 659 **OMNO2 v4 (orange squares) and GOME-2 GDP 4.8 (green squares), respectively.**

660 Figure 12b-d show the comparison of NO<sub>2</sub> diurnal variations for different groups of MEE sites. The  
 661 diurnal variations of POMINO-GEMS derived surface NO<sub>2</sub> concentrations show similar characteristics  
 662 over urban, suburban and rural regions, and all correlate well with those of MEE data. Meanwhile,  
 663 surface NO<sub>2</sub> concentrations derived from LEO satellite observations also agree well with those of  
 664 POMINO-GEMS, except that POMINO-GEMS derived surface NO<sub>2</sub> concentrations are higher than

665 those of GOME-2 GDP 4.8 by about 40% – 60%. We conclude that validation with extensive MEE  
666 measurements presents promising performance of POMINO-GEMS retrievals, especially the great  
667 agreement of POMINO-GEMS NO<sub>2</sub> diurnal variation with MEE data over urban, suburban and rural  
668 regions.

### 669 **3.5 Error estimates for POMINO-GEMS tropospheric NO<sub>2</sub> VCDs**

670 Total retrieval errors for POMINO-GEMS tropospheric NO<sub>2</sub> VCDs are derived from the  
671 calculations of total SCDs, stratospheric SCDs, and tropospheric AMFs. Spatial and temporal averaging  
672 across GEMS pixels can greatly reduce the random errors, but will not affect the systematic errors. Here,  
673 we provide a preliminary estimate of POMINO-GEMS errors for the summertime retrieval discussed  
674 above.

675 As described in Section 2, we calculate hourly total SCDs based on the original GEMS SCD data  
676 and daily TROPOMI-guided corrections. According to the GEMS ATBD of NO<sub>2</sub> retrieval algorithm, the  
677 SCD errors from the DOAS method are < 5.65% at high-NO<sub>2</sub> conditions (NO<sub>2</sub> VCD > 1 × 10<sup>15</sup> molec.  
678 cm<sup>-2</sup>) (Lee et al., 2020). The NO<sub>2</sub> SCD errors of TROPOMI are reported to be 0.5 – 0.6 × 10<sup>15</sup> molec.  
679 cm<sup>-2</sup> (10% in a relative sense) (Van Geffen et al., 2022a). Given the assumption we made in adjusting  
680 GEMS total SCDs to match TROPOMI values, we tentatively estimate the error in our corrected total  
681 SCD data to be 0.5 – 0.7 × 10<sup>15</sup> molec. cm<sup>-2</sup> (10% in a relative sense) for most regions and 0.9 × 10<sup>15</sup>  
682 molec. cm<sup>-2</sup> (20% – 30%) at the edge of the northwestern GEMS FOV.

683 In constructing the stratospheric NO<sub>2</sub> SCDs, the stratospheric VCDs are taken from TROPOMI PAL  
684 v2.3.1, scaled based on GEOS-CF v1 stratospheric NO<sub>2</sub> to account for diurnal variation, and then applied  
685 with geometric AMFs. We assign a constant error of 0.2 × 10<sup>15</sup> molec. cm<sup>-2</sup> (5% – 10%) to our hourly  
686 stratospheric SCDs, the same as the value for TROPOMI (Van Geffen et al., 2022a). Few studies have  
687 assessed the accuracy of stratospheric NO<sub>2</sub> and its diurnal variation from GEOS-CF data (Knowland et  
688 al., 2022b), but our comparison between GEOS-CF and TROPOMI shows great consistency (Section  
689 2.1.5). As most of the errors in total SCDs are absorbed in the stratosphere-troposphere separation step  
690 (Van Geffen et al., 2015), the errors in tropospheric SCDs should be 10% – 30% depending on different  
691 cases, with higher relative biases in cleaner situations.

692 Tropospheric AMF calculations are the dominant error source for retrieved tropospheric NO<sub>2</sub> VCDs  
693 over polluted regions. According to Liu et al. (2020), the AMF errors caused by uncertainty in surface

694 reflectance are about 10%, and errors induced by uncertainties in aerosol parameters are about 10% in  
695 clean regions and 20% for heavily polluted situations. We further assume that the O<sub>2</sub>-O<sub>2</sub> cloud retrieval  
696 algorithm introduces another error at the 10% level to the NO<sub>2</sub> AMFs. The uncertainty in a priori NO<sub>2</sub>  
697 vertical profiles is estimated to cause an AMF error by 10% (Liu et al., 2020). Yang et al. (2023)  
698 suggested that the NO<sub>2</sub> profiles from GEOS-Chem (version 13.3.4) might contain incorrect timing of  
699 PBL mixing growth in the morning and thus introduce a relative root-mean-square error of 7.6% and  
700 NMB of 2.7% in AMF; however, this error could be greatly dampened by averaging over a long time  
701 period. The free tropospheric NO<sub>2</sub> bias in GEOS-Chem NO<sub>2</sub> profiles might also contribute to the retrieval  
702 errors especially over remote regions. Adding these errors in quadrature leads to the overall AMF errors  
703 for POMINO-GEMS at 20% – 40%.

704 The overall uncertainty in POMINO-GEMS tropospheric NO<sub>2</sub> VCDs is estimated by adding in  
705 quadrature the errors in tropospheric NO<sub>2</sub> SCDs and AMFs, when these errors are expressed in the  
706 relative sense. For remote regions with low tropospheric NO<sub>2</sub> abundances, the overall retrieval  
707 uncertainties can reach 30% – 50% and are dominated by errors in tropospheric SCDs. For regions with  
708 abundant tropospheric NO<sub>2</sub>, the uncertainties of retrieved tropospheric VCDs are dominated by the AMF  
709 errors and are estimated to be about 20% – 30%.

710 As shown in Figure 8d and Figure 11d, the maximum negative NMB of POMINO-GEMS  
711 tropospheric NO<sub>2</sub> VCDs relative to ground-based MAX-DOAS data is about 20% in the mid-morning,  
712 and the NMB of POMINO-GEMS derived surface NO<sub>2</sub> concentrations to MEE measurements is –30%  
713 on average. Thus our estimated error magnitude is supported by the independent ground-based MAX-  
714 DOAS and MEE data.

#### 715 **4. Conclusions**

716 The GEMS instrument provides an unprecedented opportunity for air quality monitoring at a high  
717 spatiotemporal resolution. Our POMINO-GEMS algorithm retrieves tropospheric NO<sub>2</sub> VCDs as a  
718 research product. The algorithm first calculates hourly tropospheric NO<sub>2</sub> SCDs through fusion of total  
719 NO<sub>2</sub> SCDs from the GEMS v1.0 L2 NO<sub>2</sub> product, total and stratospheric NO<sub>2</sub> columns from the  
720 TROPOMI PAL v2.3.1 L2 NO<sub>2</sub> product, and stratospheric NO<sub>2</sub> diurnal variations from the GEOS-CF v1  
721 dataset. The fusion approach reduces the high bias in total SCDs and removes the stripe-like patterns in  
722 the official GEMS v1.0 product. Our algorithm then calculates tropospheric NO<sub>2</sub> AMFs to convert SCDs

723 to VCDs. A preliminary estimate of retrieval errors is also given.

724 Our initial POMINO-GEMS data for JJA 2021 shows high values of tropospheric NO<sub>2</sub> VCDs with  
725 clear hotspots ( $> 10 \times 10^{15}$  molec. cm<sup>-2</sup>) over regions where anthropogenic emissions of NO<sub>x</sub> are abundant.  
726 The spatial gradients of tropospheric NO<sub>2</sub> VCDs from urban centers to surrounding areas are substantial  
727 in the morning due to traffic emissions, but the gradients are much reduced at noon and in the afternoon.  
728 A gradual increase of tropospheric NO<sub>2</sub> VCDs from the morning to noon is observed over clean regions  
729 of western China, likely as a result of enhanced biogenic emissions. Over high NO<sub>2</sub> regions where  
730 anthropogenic activities dominate the NO<sub>x</sub> emissions, NO<sub>2</sub> columns increase until a peak at 09:00 – 10:00  
731 LST, decrease to the minimum at noon and then increase in the afternoon again. Such characteristics of  
732 NO<sub>2</sub> diurnal variations are associated with the changes in natural and anthropogenic NO<sub>x</sub> emissions,  
733 photochemistry and atmospheric transport.

734 POMINO-GEMS tropospheric NO<sub>2</sub> VCDs agree well with POMINO-TROPOMI v1.2.2 in terms of  
735 spatial correlation (0.98) and NMB (4.9%). POMINO-GEMS data are also consistent with the OMNO2  
736 v4 tropospheric NO<sub>2</sub> VCD product in the early afternoon and GOME-2 GDP 4.8 tropospheric NO<sub>2</sub> VCD  
737 product in the morning, with *R* of 0.87 and 0.83, and NMB of -16.8% and -1.5%, respectively.

738 POMINO-GEMS tropospheric NO<sub>2</sub> VCDs are comparable with ground-based MAX-DOAS  
739 measurements at nine ground-based sites with a small NMB (-11.1%), although the correlation is modest  
740 (*R* = 0.66). Both the bias and correlation values are smaller than POMINO-TROPOMI v1.2.2 (NMB =  
741 -18.1%, *R* = 0.83). More importantly, POMINO-GEMS well captures the diurnal variation of MAX-  
742 DOAS NO<sub>2</sub> VCDs at Xuzhou (*R* = 0.82), Hefei (*R* = 0.96), Fudan University (*R* = 0.84), Nanhui (*R* =  
743 0.79), Xianghe (*R* = 0.94) and Dianshan Lake (*R* = 0.60) sites, although the correlations are relatively  
744 poor at Chongming and Fukue sites. Comparison with mobile-car MAX-DOAS measurements in the  
745 Three Rivers' Source region on the Tibetan Plateau also shows good correlation in NO<sub>2</sub> diurnal variation  
746 (*R* = 0.81).

747 We also compare surface NO<sub>2</sub> concentrations derived from tropospheric NO<sub>2</sub> VCDs in POMINO-  
748 GEMS and POMINO-TROPOMI v1.2.2 against MEE data, taking advantage of the large number of  
749 MEE sites. POMINO-GEMS derived surface NO<sub>2</sub> concentration data exhibit a small NMB (-26.3%).  
750 For these sites at TROPOMI overpass times, POMINO-GEMS derived surface NO<sub>2</sub> concentrations show  
751 a smaller magnitude of NMB (-48.0%) than POMINO-TROPOMI v1.2.2 (-55.8%). Excellent

752 agreement in diurnal variation between POMINO-GEMS derived and MEE NO<sub>2</sub> is exhibited over all (*R*  
753 = 0.97), urban (*R* = 0.97), suburban (*R* = 0.97) and rural (*R* = 0.96) sites.

754 Overall, our comprehensive validation process highlights the good performance of POMINO-  
755 GEMS tropospheric NO<sub>2</sub> VCD product, both in magnitude and spatiotemporal variation. However, there  
756 are still several limitations in our study. To address the systematic overestimation and stripes problems  
757 in the original GEMS data, we correct GEMS total NO<sub>2</sub> SCDs by using TROPOMI data as a temporary  
758 solution. For example, we implement a simple geometric correction to combine GEMS and TROPOMI  
759 total NO<sub>2</sub> SCDs, but their differences in scattering geometry are only partly accounted for. Thus this  
760 correction works well in most regions, but may introduce SCD uncertainties up to  $0.9 \times 10^{15}$  molec. cm<sup>-2</sup>  
761 (20% – 30%) at the edge of the northwestern GEMS FOV. Currently, the Environmental Satellite Center  
762 of South Korea is updating the NO<sub>2</sub> SCD data to v2.0. We will update our POMINO-GEMS algorithm  
763 accordingly, once the updated official NO<sub>2</sub> product becomes available to provide necessary inputs for  
764 our research product. In addition, in the conversion from NO<sub>2</sub> VCDs to surface concentrations, we use a  
765 constant correction factor of 2 to account for the strong NO<sub>2</sub> vertical gradient near the surface. This  
766 simple treatment does not account for the diurnal variation of the correction factor, and thus may  
767 introduce errors in the derived surface NO<sub>2</sub> concentrations. Nevertheless, the current POMINO-GEMS  
768 data serve as our initial attempt to derive the diurnal variations of tropospheric NO<sub>2</sub> at a high  
769 spatiotemporal resolution from GEMS, and they are expected to offer a useful source of information for  
770 various applications such as air quality analysis and emission constraint.

771

772 *Data availability.* The POMINO-GEMS NO<sub>2</sub> data will be freely available soon at the ACM group  
773 product website (<http://www.pku-atmos-acm.org/acmProduct.php/>). The TROPOMI PAL v2.3.1 L2  
774 product can be downloaded from <https://data-portal.s5p-pal.com>. The OMNO2 v4 L2 product can be  
775 downloaded from [https://aura.gesdisc.eosdis.nasa.gov/data/Aura\\_OMI\\_Level2/OMNO2.003/](https://aura.gesdisc.eosdis.nasa.gov/data/Aura_OMI_Level2/OMNO2.003/). The  
776 GOME-2 GDP 4.8 L2 product can be downloaded from <http://acsaf.org/> after registration. The GEOS-  
777 CF v1.0 dataset can be downloaded from [https://gmao.gsfc.nasa.gov/weather\\_prediction/GEOS-  
778 CF/data\\_access/](https://gmao.gsfc.nasa.gov/weather_prediction/GEOS-CF/data_access/). The MEE surface NO<sub>2</sub> measurements can be downloaded from <https://quotsoft.net/air/>.  
779 The ground-based and mobile-car MAX-DOAS measurements can be provided upon requests to the  
780 corresponding owners.

781

782 *Author contributions.* JL conceived this research. YZ and JL designed the algorithm and validation  
783 process. YZ performed all calculations with additional code support from HK. YZ and JL wrote the paper.  
784 RS provided LIDORT. JK, HL, JP and HH provided GEMS data. MVR, FH, TiW, PW, QH, KQ, YC,  
785 YK, JX, PX, XT, SZ and SW provided the ground-based MAX-DOAS measurements. SC, XC, JM and  
786 ThW provided the mobile-car MAX-DOAS measurements. HK helped process MEE measurements. LC  
787 and ML helped analyze the validation results. All authors commented on the paper.

788

789 *Competing interests.* The authors declare that they have no conflicts of interest.

790

791 *Financial support.* This research has been supported by the National Natural Science Foundation of  
792 China (grant no. 42075175) and the Second Tibetan Plateau Scientific Expedition and Research Program  
793 (grant no. 2019QZKK0604).

794

## 795 **References**

796 Beirle, S., Boersma, K. F., Platt, U., Lawrence, M. G., and Wagner, T.: Megacity Emissions and  
797 Lifetimes of Nitrogen Oxides Probed from Space, *Science*, 333, 1737-1739, 10.1126/science.1207824,  
798 2011.

799 Biswas, M. S. and Mahajan, A. S.: Year-long Concurrent MAX-DOAS Observations of Nitrogen  
800 Dioxide and Formaldehyde at Pune: Understanding Diurnal and Seasonal Variation Drivers, *Aerosol and*  
801 *Air Quality Research*, 21, 200524, 10.4209/aaqr.200524, 2021.

802 Boersma, K. F., Eskes, H. J., and Brinksma, E. J.: Error analysis for tropospheric NO<sub>2</sub> retrieval from  
803 space, *Journal of Geophysical Research: Atmospheres*, 109, n/a-n/a, 10.1029/2003jd003962, 2004.

804 Boersma, K. F., Jacob, D. J., Eskes, H. J., Pinder, R. W., Wang, J., and Van Der A, R. J.:  
805 Intercomparison of SCIAMACHY and OMI tropospheric NO<sub>2</sub> columns: Observing the  
806 diurnal evolution of chemistry and emissions from space, *Journal of Geophysical Research*, 113,  
807 10.1029/2007jd008816, 2008.

808 Boersma, K. F., Jacob, D. J., Trainic, M., Rudich, Y., Desmedt, I., Dirksen, R., and Eskes, H. J.:  
809 Validation of urban NO<sub>2</sub> concentrations and their diurnal and seasonal variations observed



810 from the SCIAMACHY and OMI sensors using in situ surface measurements in Israeli cities,  
811 Atmospheric Chemistry and Physics, 9, 3867-3879, 10.5194/acp-9-3867-2009, 2009.

812 Boersma, K. F., Eskes, H. J., Dirksen, R. J., van der A, R. J., Veefkind, J. P., Stammes, P., Huijnen,  
813 V., Kleipool, Q. L., Sneep, M., Claas, J., Leitão, J., Richter, A., Zhou, Y., and Brunner, D.: An improved  
814 tropospheric NO<sub>2</sub> column retrieval algorithm for the Ozone Monitoring Instrument, Atmospheric  
815 Measurement Techniques, 4, 1905-1928, 10.5194/amt-4-1905-2011, 2011.

816 Burrows, J. P.: The Global Ozone Monitoring Experiment (GOME) : Mission concept and first  
817 scientific results, Journal of Atmospheric Sciences, 56, 2340-2352, 1999.

818 Callies, J., Corpaccioli, E., Eisinger, M., Hahne, A., and Lefebvre, A.: GOME-2 – Metop ' s Second-  
819 Generation Sensor for Operational Ozone Monitoring,

820 Chen, L., Lin, J., Martin, R., Du, M., Weng, H., Kong, H., Ni, R., Meng, J., Zhang, Y., Zhang, L.,  
821 and van Donkelaar, A.: Inequality in historical transboundary anthropogenic PM<sub>2.5</sub> health impacts,  
822 Science Bulletin, <https://doi.org/10.1016/j.scib.2021.11.007>, 2021.

823 Chen, L., Lin, J., Ni, R., Kong, H., Du, M., Yan, Y., Liu, M., Wang, J., Weng, H., Zhao, Y., Li, C.,  
824 and Martin, R. V.: Historical transboundary ozone health impact linked to affluence, Environmental  
825 Research Letters, 17, 104014, 10.1088/1748-9326/ac9009, 2022.

826 Cheng, S., Cheng, X., Ma, J., Xu, X., Zhang, W., Lv, J., Bai, G., Chen, B., Ma, S., Ziegler, S.,  
827 Donner, S., and Wagner, T.: Mobile MAX-DOAS observations of tropospheric NO<sub>2</sub> and HCHO during  
828 summer over the Three Rivers' Source region in China, Atmos. Chem. Phys., 23, 3655-3677,  
829 10.5194/acp-23-3655-2023, 2023.

830 Cooper, M. J., Martin, R. V., Hammer, M. S., Levelt, P. F., Veefkind, P., Lamsal, L. N., Krotkov, N.  
831 A., Brook, J. R., and McInden, C. A.: Global fine-scale changes in ambient NO<sub>2</sub> during COVID-19  
832 lockdowns, Nature, 601, 380-387, 10.1038/s41586-021-04229-0, 2022.

833 Crutzen, P. J.: The influence of nitrogen oxides on the atmospheric ozone content, Quarterly Journal  
834 of the Royal Meteorological Society, 96, 320-325, 10.1002/qj.49709640815, 1970.

835 Cui, Y., Lin, J., Song, C., Liu, M., Yan, Y., Xu, Y., and Huang, B.: Rapid growth in nitrogen dioxide  
836 pollution over Western China, 2005–2013, Atmos. Chem. Phys., 16, 6207-6221, 10.5194/acp-16-6207-  
837 2016, 2016.

838 Dirksen, R. J., Boersma, K. F., Eskes, H. J., Ionov, D. V., Bucsela, E. J., Levelt, P. F., and Kelder, H.

839 M.: Evaluation of stratospheric NO<sub>2</sub> retrieved from the Ozone Monitoring Instrument: Intercomparison,  
840 diurnal cycle, and trending, *Journal of Geophysical Research*, 116, 10.1029/2010jd014943, 2011.

841 Eastham, S. D., Weisenstein, D. K., and Barrett, S. R. H.: Development and evaluation of the unified  
842 tropospheric–stratospheric chemistry extension (UCX) for the global chemistry-transport model GEOS-  
843 Chem, *Atmospheric Environment*, 89, 52-63, <https://doi.org/10.1016/j.atmosenv.2014.02.001>, 2014.

844 Eskes, H., Van Geffen, J., Sneep, M., Veefkind, P., Niemeier, S., and Zehner, C.: S5P Nitrogen  
845 Dioxide v02.03.01 intermediate reprocessing on the S5P-PAL system: Readme file, 2021.

846 Ghude, S. D., Karumuri, R. K., Jena, C., Kulkarni, R., Pfister, G. G., Sajjan, V. S., Pithani, P.,  
847 Debnath, S., Kumar, R., Upendra, B., Kulkarni, S. H., Lal, D. M., Vander A, R. J., and Mahajan, A. S.:  
848 What is driving the diurnal variation in tropospheric NO<sub>2</sub> columns over a cluster of high emission  
849 thermal power plants in India?, *Atmospheric Environment: X*, 5, 100058,  
850 <https://doi.org/10.1016/j.aeaoa.2019.100058>, 2020.

851 Grubbs, F. E.: Sample Criteria for Testing Outlying Observations, *The Annals of Mathematical*  
852 *Statistics*, 21, 27-58, 10.1214/aoms/1177729885, 1950.

853 Gu, D., Wang, Y., Smeltzer, C., and Boersma, K. F.: Anthropogenic emissions of NO<sub>x</sub> over China:  
854 Reconciling the difference of inverse modeling results using GOME-2 and OMI measurements, *Journal*  
855 *of Geophysical Research: Atmospheres*, 119, 7732-7740, 10.1002/2014jd021644, 2014.

856 Hendrick, F., Müller, J.-F., Clémer, K., Wang, P., De Mazière, M., Fayt, C., Gielen, C., Hermans, C.,  
857 Ma, J. Z., Pinardi, G., Stavrou, T., Vlemmix, T., and Van Roozendaal, M.: Four years of ground-based  
858 MAX-DOAS observations of HONO and NO<sub>2</sub> in the Beijing area, *Atmospheric Chemistry*  
859 *and Physics*, 14, 765-781, 10.5194/acp-14-765-2014, 2014.

860 Herman, J., Abuhassan, N., Kim, J., Kim, J., Dubey, M., Raponi, M., and Tzortziou, M.:  
861 Underestimation of column NO<sub>2</sub> amounts from the OMI satellite compared to diurnally varying ground-  
862 based retrievals from multiple PANDORA spectrometer instruments, *Atmos. Meas. Tech.*, 12, 5593-5612,  
863 10.5194/amt-12-5593-2019, 2019.

864 Hoek, G., Krishnan, R. M., Beelen, R., Peters, A., Ostro, B., Brunekreef, B., and Kaufman, J. D.:  
865 Long-term air pollution exposure and cardio- respiratory mortality: a review, *Environmental Health*, 12,  
866 43, 10.1186/1476-069X-12-43, 2013.

867 Jing, B., Wu, L., Mao, H., Gong, S., He, J., Zou, C., Song, G., Li, X., and Wu, Z.: Development of

868 a vehicle emission inventory with high temporal–spatial resolution based on NRT traffic data and its  
869 impact on air pollution in Beijing – Part 1: Development and evaluation of vehicle emission inventory,  
870 *Atmospheric Chemistry and Physics*, 16, 3161-3170, 10.5194/acp-16-3161-2016, 2016.

871 Kanaya, Y., Irie, H., Takashima, H., Iwabuchi, H., Akimoto, H., Sudo, K., Gu, M., Chong, J., Kim,  
872 Y. J., Lee, H., Li, A., Si, F., Xu, J., Xie, P.-H., Liu, W.-Q., Dzhola, A., Posttyakov, O., Ivanov, V.,  
873 Grechko, E., Terpugova, S., and Panchenko, M.: Long-term MAX-DOAS network observations of  
874 NO<sub>2</sub> in Russia and Asia (MADRAS) during the period 2007–2012: instrumentation,  
875 elucidation of climatology, and comparisons with OMI satellite observations and global model si,  
876 *Atmospheric Chemistry and Physics*, 14, 7909-7927, 10.5194/acp-14-7909-2014, 2014.

877 Keller, C. A., Knowland, K. E., Duncan, B. N., Liu, J., Anderson, D. C., Das, S., Lucchesi, R. A.,  
878 Lundgren, E. W., Nicely, J. M., Nielsen, E., Ott, L. E., Saunders, E., Strode, S. A., Wales, P. A., Jacob, D.  
879 J., and Pawson, S.: Description of the NASA GEOS Composition Forecast Modeling System GEOS-CF  
880 v1.0, *Journal of Advances in Modeling Earth Systems*, 13, 10.1029/2020ms002413, 2021.

881 Kim, J., Jeong, U., Ahn, M.-H., Kim, J. H., Park, R. J., Lee, H., Song, C. H., Choi, Y.-S., Lee, K.-  
882 H., Yoo, J.-M., Jeong, M.-J., Park, S. K., Lee, K.-M., Song, C.-K., Kim, S.-W., Kim, Y. J., Kim, S.-W.,  
883 Kim, M., Go, S., Liu, X., Chance, K., Chan Miller, C., Al-Saadi, J., Veihelmann, B., Bhartia, P. K., Torres,  
884 O., Abad, G. G., Haffner, D. P., Ko, D. H., Lee, S. H., Woo, J.-H., Chong, H., Park, S. S., Nicks, D., Choi,  
885 W. J., Moon, K.-J., Cho, A., Yoon, J., Kim, S.-K., Hong, H., Lee, K., Lee, H., Lee, S., Choi, M., Veefkind,  
886 P., Levelt, P. F., Edwards, D. P., Kang, M., Eo, M., Bak, J., Baek, K., Kwon, H.-A., Yang, J., Park, J.,  
887 Han, K. M., Kim, B.-R., Shin, H.-W., Choi, H., Lee, E., Chong, J., Cha, Y., Koo, J.-H., Irie, H., Hayashida,  
888 S., Kasai, Y., Kanaya, Y., Liu, C., Lin, J., Crawford, J. H., Carmichael, G. R., Newchurch, M. J., Lefter,  
889 B. L., Herman, J. R., Swap, R. J., Lau, A. K. H., Kurosu, T. P., Jaross, G., Ahlers, B., Dobber, M., McElroy,  
890 C. T., and Choi, Y.: New Era of Air Quality Monitoring from Space: Geostationary Environment  
891 Monitoring Spectrometer (GEMS), *Bulletin of the American Meteorological Society*, 101, E1-E22,  
892 10.1175/bams-d-18-0013.1, 2020.

893 Kim, S., Kim, D., Hong, H., Chang, L. S., Lee, H., Kim, D. R., Kim, D., Yu, J. A., Lee, D., Jeong,  
894 U., Song, C. K., Kim, S. W., Park, S. S., Kim, J., Hanisco, T. F., Park, J., Choi, W., and Lee, K.: First-  
895 time comparison between NO<sub>2</sub> vertical columns from GEMS and Pandora measurements, *Atmos. Meas.*  
896 *Tech. Discuss.*, 2023, 1-22, 10.5194/amt-2023-11, 2023.

897 Knowland, K. E., Keller, C. A., and Lucchesi, R. A.: File Specification for GEOS-CF Products,  
898 2022a.

899 Knowland, K. E., Keller, C. A., Wales, P. A., Wargan, K., Coy, L., Johnson, M. S., Liu, J., Lucchesi,  
900 R. A., Eastham, S. D., Fleming, E., Liang, Q., Leblanc, T., Livesey, N. J., Walker, K. A., Ott, L. E., and  
901 Pawson, S.: NASA GEOS Composition Forecast Modeling System GEOS-CF v1.0: Stratospheric  
902 Composition, *Journal of Advances in Modeling Earth Systems*, 14, e2021MS002852,  
903 <https://doi.org/10.1029/2021MS002852>, 2022b.

904 Kong, H., Lin, J., Chen, L., Zhang, Y., Yan, Y., Liu, M., Ni, R., Liu, Z., and Weng, H.: Considerable  
905 Unaccounted Local Sources of NO<sub>x</sub> Emissions in China Revealed from Satellite, *Environmental Science*  
906 *& Technology*, 56, 7131-7142, 10.1021/acs.est.1c07723, 2022a.

907 Kong, H., Lin, J., Zhang, Y., Li, C., Xu, C., Shen, L., Liu, X., Yang, K., Su, H., and Xu, W.:  
908 Unexpected high NO<sub>x</sub> emissions from lakes on Tibetan Plateau under rapid warming, 10.21203/rs.3.rs-  
909 1980236/v1, 2022b.

910 Kong, H., Lin, J., Zhang, Y., Li, C., Xu, C., Shen, L., Liu, X., Yang, K., Su, H., and Xu, W.: High  
911 natural nitric oxide emissions from lakes on Tibetan Plateau under rapid warming, *Nature Geoscience*,  
912 16, 474-477, 10.1038/s41561-023-01200-8, 2023.

913 Krotkov, N. A., McLinden, C. A., Li, C., Lamsal, L. N., Celarier, E. A., Marchenko, S. V., Swartz,  
914 W. H., Bucsela, E. J., Joiner, J., Duncan, B. N., Boersma, K. F., Veefkind, J. P., Levelt, P. F., Fioletov, V.  
915 E., Dickerson, R. R., He, H., Lu, Z., and Streets, D. G.: Aura OMI observations of regional SO<sub>2</sub> and NO<sub>2</sub>  
916 pollution changes from 2005 to 2015, *Atmos. Chem. Phys.*, 16, 4605-4629, 10.5194/acp-16-4605-2016,  
917 2016.

918 Lamsal, L. N., Krotkov, N. A., Vasilkov, A., Marchenko, S., Qin, W., Yang, E.-S., Fasnacht, Z.,  
919 Joiner, J., Choi, S., Haffner, D., Swartz, W. H., Fisher, B., and Bucsela, E.: Ozone Monitoring Instrument  
920 (OMI) Aura nitrogen dioxide standard product version 4.0 with improved surface and cloud treatments,  
921 *Atmospheric Measurement Techniques*, 14, 455-479, 10.5194/amt-14-455-2021, 2021.

922 Lee, H., Park, J., and Hong, H.: Geostationary Environment Monitoring Spectrometer (GEMS)  
923 Algorithm Theoretical Basis Document NO<sub>2</sub> Retrieval Algorithm, 2020.

924 Lee, Y., Ahn, M. H., Kang, M., and Eo, M.: Spectral replacement using machine learning methods  
925 for continuous mapping of the Geostationary Environment Monitoring Spectrometer (GEMS), *Atmos.*

926 Meas. Tech., 16, 153-168, 10.5194/amt-16-153-2023, 2023.

927 Levelt, P. F., Van Den Oord, G. H. J., Dobber, M. R., Malkki, A., Visser, H., Vries, J. D., Stammes,  
928 P., Lundell, J. O. V., and Saari, H.: The ozone monitoring instrument, IEEE Transactions on Geoscience  
929 and Remote Sensing, 44, 1093-1101, 10.1109/tgrs.2006.872333, 2006.

930 Li, J., Wang, Y., Zhang, R., Smeltzer, C., Weinheimer, A., Herman, J., Boersma, K. F., Celarier, E.  
931 A., Long, R. W., Szykman, J. J., Delgado, R., Thompson, A. M., Knepp, T. N., Lamsal, L. N., Janz, S. J.,  
932 Kowalewski, M. G., Liu, X., and Nowlan, C. R.: Comprehensive evaluations of diurnal NO<sub>2</sub>  
933 measurements during DISCOVER-AQ 2011: effects of resolution-dependent representation of NO<sub>x</sub>  
934 emissions, Atmos. Chem. Phys., 21, 11133-11160, 10.5194/acp-21-11133-2021, 2021a.

935 Li, K.-F., Khoury, R., Pongetti, T. J., Sander, S. P., Mills, F. P., and Yung, Y. L.: Diurnal variability  
936 of stratospheric column NO<sub>2</sub> measured using direct solar and lunar spectra over Table  
937 Mountain, California (34.38° N), Atmospheric Measurement Techniques, 14, 7495-7510, 10.5194/amt-  
938 14-7495-2021, 2021b.

939 Lin, J. T. and McElroy, M. B.: Detection from space of a reduction in anthropogenic emissions of  
940 nitrogen oxides during the Chinese economic downturn, Atmos. Chem. Phys., 11, 8171-8188,  
941 10.5194/acp-11-8171-2011, 2011.

942 Lin, J. T., Liu, M. Y., Xin, J. Y., Boersma, K. F., Spurr, R., Martin, R., and Zhang, Q.: Influence of  
943 aerosols and surface reflectance on satellite NO<sub>2</sub> retrieval: seasonal and spatial characteristics and  
944 implications for NO<sub>x</sub> emission constraints, Atmospheric Chemistry and Physics, 15, 11217-11241,  
945 10.5194/acp-15-11217-2015, 2015.

946 Lin, J. T., Martin, R. V., Boersma, K. F., Sneep, M., Stammes, P., Spurr, R., Wang, P., Van  
947 Roozendaal, M., Clémer, K., and Irie, H.: Retrieving tropospheric nitrogen dioxide from the Ozone  
948 Monitoring Instrument: effects of aerosols, surface reflectance anisotropy, and vertical profile of nitrogen  
949 dioxide, Atmospheric Chemistry and Physics, 14, 1441-1461, 10.5194/acp-14-1441-2014, 2014.

950 Liu, M., Lin, J., Wang, Y., Sun, Y., Zheng, B., Shao, J., Chen, L., Zheng, Y., Chen, J., Fu, T. M., Yan,  
951 Y., Zhang, Q., and Wu, Z.: Spatiotemporal variability of NO<sub>2</sub> and PM<sub>2.5</sub> over Eastern China:  
952 observational and model analyses with a novel statistical method, Atmos. Chem. Phys., 18, 12933-12952,  
953 10.5194/acp-18-12933-2018, 2018a.

954 Liu, M., Lin, J., Kong, H., Boersma, K. F., Eskes, H., Kanaya, Y., He, Q., Tian, X., Qin, K., Xie, P.,

955 Spurr, R., Ni, R., Yan, Y., Weng, H., and Wang, J.: A new TROPOMI product for tropospheric NO<sub>2</sub>  
956 columns over East Asia with explicit aerosol corrections, *Atmos. Meas. Tech.*, 13, 4247-4259,  
957 10.5194/amt-13-4247-2020, 2020.

958 Liu, M., Lin, J., Boersma, K. F., Pinardi, G., Wang, Y., Chimot, J., Wagner, T., Xie, P., Eskes, H.,  
959 Van Roozendael, M., Hendrick, F., Wang, P., Wang, T., Yan, Y., Chen, L., and Ni, R.: Improved aerosol  
960 correction for OMI tropospheric NO<sub>2</sub> retrieval over East Asia: constraint from CALIOP aerosol vertical  
961 profile, *Atmospheric Measurement Techniques*, 12, 1-21, 10.5194/amt-12-1-2019, 2019.

962 Liu, Y.-H., Ma, J.-L., Li, L., Lin, X.-F., Xu, W.-J., and Ding, H.: A high temporal-spatial vehicle  
963 emission inventory based on detailed hourly traffic data in a medium-sized city of China, *Environmental*  
964 *Pollution*, 236, 324-333, <https://doi.org/10.1016/j.envpol.2018.01.068>, 2018b.

965 Lorente, A., Boersma, K. F., Stammes, P., Tilstra, L. G., and Muller, J. P.: The importance of surface  
966 reflectance anisotropy for cloud and NO<sub>2</sub> retrievals from GOME-2 and OMI, 2018.

967 Lorente, A., Boersma, K. F., Yu, H., Dorner, S., Hilboll, A., Richter, A., Liu, M., Lamsal, L. N.,  
968 Barkley, M. P., and De Smedt, I.: Structural uncertainty in air mass factor calculation for NO<sub>2</sub> and HCHO  
969 satellite retrievals, *Atmospheric Measurement Techniques*, 10, 759-782, 2016.

970 Lucht, W., Schaaf, C. B., and Strahler, A. H.: An algorithm for the retrieval of albedo from space  
971 using semiempirical BRDF models, *IEEE Transactions on Geoscience & Remote Sensing*, 38, 977-998,  
972 2000.

973 Naiudomthum, S., Winijkul, E., and Sirisubtawee, S.: Near Real-Time Spatial and Temporal  
974 Distribution of Traffic Emissions in Bangkok Using Google Maps Application Program Interface,  
975 *Atmosphere*, 13, 1803, 10.3390/atmos13111803, 2022.

976 Palmer, P. I., Jacob, D. J., Chance, K., Martin, R. V., Spurr, R. J. D., Kurosu, T. P., Bey, I., Yantosca,  
977 R., Fiore, A., and Li, Q.: Air mass factor formulation for spectroscopic measurements from satellites:  
978 Application to formaldehyde retrievals from the Global Ozone Monitoring Experiment, *Journal of*  
979 *Geophysical Research: Atmospheres*, 106, 14539-14550, 10.1029/2000jd900772, 2001.

980 Richter, A., Burrows, J. P., Nüß, H., Granier, C., and Niemeier, U.: Increase in tropospheric nitrogen  
981 dioxide over China observed from space, *Nature*, 437, 129-132, 10.1038/nature04092, 2005.

982 Shindell, D. T., Faluvegi, G., Koch, D. M., Schmidt, G. A., Unger, N., and Bauer, S. E.: Improved  
983 Attribution of Climate Forcing to Emissions, *Science*, 326, 716-718, 10.1126/science.1174760, 2009.

984 Valks, P.: Algorithm Theoretical Basis Document for GOME-2 Total Column Products of Ozone,  
985 NO<sub>2</sub>, BrO, SO<sub>2</sub>, H<sub>2</sub>O, HCHO, OCIO and Cloud Properties (GDP 4.8/4.9), 2019.

986 Valks, P., Chan, L., Zimmer, W., Hedelt, P., and Slijkhuis, S.: PRODUCT USER MANUAL GOME-  
987 2 Total Column Products of Ozone, NO<sub>2</sub>, BrO, HCHO, SO<sub>2</sub>, H<sub>2</sub>O, OCIO and Cloud Properties GDP 4.8  
988 for GOME-2 on MetOp-A and -B GDP 4.9 for GOME-2 on MetOp-C, 2019.

989 van der A, R. J., Mijling, B., Ding, J., Koukouli, M. E., Liu, F., Li, Q., Mao, H., and Theys, N.:  
990 Cleaning up the air: effectiveness of air quality policy for SO<sub>2</sub> and NO<sub>x</sub> emissions in China, *Atmos.*  
991 *Chem. Phys.*, 17, 1775-1789, 10.5194/acp-17-1775-2017, 2017.

992 Van Geffen, J., Eskes, H., Boersma, K. F., and Veefkind, P.: TROPOMI ATBD of the total and  
993 tropospheric NO<sub>2</sub> data products, 2022a.

994 Van Geffen, J., Eskes, H., Compernelle, S., Pinardi, G., Verhoelst, T., Lambert, J.-C., Sneep, M.,  
995 Ter Linden, M., Ludewig, A., Boersma, K. F., and Veefkind, J. P.: Sentinel-5P TROPOMI  
996 NO<sub>2</sub> retrieval: impact of version v2.2 improvements and comparisons with OMI and  
997 ground-based data, *Atmospheric Measurement Techniques*, 15, 2037-2060, 10.5194/amt-15-2037-2022,  
998 2022b.

999 van Geffen, J. H. G. M., Boersma, K. F., Van Roozendaal, M., Hendrick, F., Mahieu, E., De Smedt,  
1000 I., Sneep, M., and Veefkind, J. P.: Improved spectral fitting of nitrogen dioxide from OMI in the 405–  
1001 465 nm window, *Atmos. Meas. Tech.*, 8, 1685-1699, 10.5194/amt-8-1685-2015, 2015.

1002 Vasilkov, A., Krotkov, N., Yang, E. S., Lamsal, L., Joiner, J., Castellanos, P., Fasnacht, Z., and Spurr,  
1003 R.: Explicit and consistent aerosol correction for visible wavelength satellite cloud and nitrogen dioxide  
1004 retrievals based on optical properties from a global aerosol analysis, *Atmos. Meas. Tech.*, 14, 2857-2871,  
1005 10.5194/amt-14-2857-2021, 2021.

1006 Vasilkov, A. P., Qin, W., Krotkov, N. A., Lamsal, L. N., Spurr, R., Haffner, D. P., Joiner, J., Yang,  
1007 E., and Marchenko, S.: Accounting for the Effects of Surface BRDF on Satellite Cloud and Trace-Gas  
1008 Retrievals: A New Approach Based on Geometry-Dependent Lambertian-Equivalent Reflectivity  
1009 Applied to OMI Algorithms, *Atmospheric Measurement Techniques*, 10, 333-349, 2016.

1010 Veefkind, J. P., Aben, I., McMullan, K., Förster, H., de Vries, J., Otter, G., Claas, J., Eskes, H. J., de  
1011 Haan, J. F., Kleipool, Q., van Weele, M., Hasekamp, O., Hoogeveen, R., Landgraf, J., Snel, R., Tol, P.,  
1012 Ingmann, P., Voors, R., Kruizinga, B., Vink, R., Visser, H., and Levelt, P. F.: TROPOMI on the ESA

1013 Sentinel-5 Precursor: A GMES mission for global observations of the atmospheric composition for  
1014 climate, air quality and ozone layer applications, *Remote Sensing of Environment*, 120, 70-83,  
1015 <https://doi.org/10.1016/j.rse.2011.09.027>, 2012.

1016 Wei, J., Liu, S., Li, Z., Liu, C., Qin, K., Liu, X., Pinker, R. T., Dickerson, R. R., Lin, J., Boersma,  
1017 K. F., Sun, L., Li, R., Xue, W., Cui, Y., Zhang, C., and Wang, J.: Ground-Level NO<sub>2</sub>  
1018 Surveillance from Space Across China for High Resolution Using Interpretable Spatiotemporally  
1019 Weighted Artificial Intelligence, *Environmental Science & Technology*, 56, 9988-9998,  
1020 10.1021/acs.est.2c03834, 2022.

1021 Weng, H., Lin, J., Martin, R., Millet, D. B., Jaeglé, L., Ridley, D., Keller, C., Li, C., Du, M., and  
1022 Meng, J.: Global high-resolution emissions of soil NO<sub>x</sub>, sea salt aerosols, and biogenic volatile organic  
1023 compounds, *Scientific Data*, 7, 148, 10.1038/s41597-020-0488-5, 2020.

1024 Yang, L. H., Jacob, D. J., Colombi, N. K., Zhai, S., Bates, K. H., Shah, V., Beaudry, E., Yantosca,  
1025 R. M., Lin, H., Brewer, J. F., Chong, H., Travis, K. R., Crawford, J. H., Lamsal, L. N., Koo, J. H., and  
1026 Kim, J.: Tropospheric NO<sub>2</sub> vertical profiles over South Korea and their relation to oxidant chemistry:  
1027 implications for geostationary satellite retrievals and the observation of NO<sub>2</sub> diurnal variation from space,  
1028 *Atmos. Chem. Phys.*, 23, 2465-2481, 10.5194/acp-23-2465-2023, 2023.

1029 Zhang, Y., Lin, J., Liu, M., Kong, H., Chen, L., Weng, H., and Li, C.: High-resolution Tropospheric  
1030 NO<sub>2</sub> Retrieval over Asia based on OMI POMINO v2.1 and Quantitative comparison with other products,  
1031 *National Remote Sensing Bulletin*, 10.11834/jrs.20221413, 2022.

1032 Zhou, Y., Brunner, D., Spurr, R. J. D., Boersma, K. F., Sneep, M., Popp, C., and Buchmann, B.:  
1033 Accounting for surface reflectance anisotropy in satellite retrievals of tropospheric NO<sub>2</sub>, *Atmospheric*  
1034 *Measurement Techniques*, 3, 1185-1203, 2010.

1035